A 1D-modelling approach for simulating the Soil-Pile Interaction mechanism in the liquefiable ground

Masoud Shadlou [a,b], Subhamoy Bhattacharya [c]

[a] School of Environment and Technology, University of Brighton, Brighton, UK

[b] Infrastructure research group, University of Southampton, Southampton, UK

[c] Department of Civil end Environmental Engineering, University of Surrey, Guildford, UK

Abstract

The discrepancies between the dynamic response obtained with "Beam on the nonlinear Winkler Foundation" method, as a 1D model, and the actual pile behaviour in the liquefiable ground have been identified and marked in the vast body of literature. In this study, a 1D formulation is presented for the soil-pile system which provided considerable insights on the physics of the soil behaviour around the pile in the liquefiable ground and its dependence on soil properties. Unlike the mechanical models that may or may not be generalizable, the presented method is controlled by the soil properties. By a concept that the pile response is mainly influenced by the response of soil located on a unit volume in the pile vicinity, a macro-element is hypothesized by introducing a volumetric constraint incorporating the soil volume changes. The nonlinearity of macro-element is coupled in between volumetric and distortional behaviours where an incremental plastic work is assumed. Hence a stiffness matrix operator is used, instead of a scalar value, to link the pile resistance components with displacement components. A hypo-elastic bounding surface model was developed in this framework to capture the complex mechanism of soil-pile interaction in the liquefiable ground and presents a very good accord with available field measurement and centrifuge study while the

computational time reduces to a couple of minutes for an earthquake excitation. An application for the presented 1D modelling approach is presented by calculating the instantaneous period and damping of the soil-pile interaction system in the liquefiable ground.

Keywords: 1D modelling, soil-pile system, macro-element, liquefiable ground, p-y curve

1. Introduction

New and existing superstructures (such as bridges and buildings) supported on pile foundations and located in sites susceptible to liquefaction and lateral spreading are required to be assessed or designed to withstand the actions of extreme loads. It is necessary to simulate the soil-pile system using a reliable method supported by realistic soil constitutive relations surrounding the pile. There is a trade-off between simplified 1D models and complex finite element method (FEM) however the demand is always high for simple-robust solutions which their results are in very good accord with available rigorous ones [1].

The behaviour of pile-supported structures in liquefiable and laterally spreading ground is a complex phenomenon. To simulate this complex problem, different methods are proposed by researchers. Fully coupled [2] nonlinear finite element method (FEM) is one of the rigorous solutions which require computationally expensive processors to run a complex geotechnical project containing a soil-pile-foundation-superstructure system under dynamic loading conditions. Using FEM for soil-pile interaction assessment in the liquefied ground has been investigated by many researchers in recent years such as [3], [4], [5], [6], [7], [8], [9], [10], [11]. The effectiveness of continuum solutions for analysing the interaction mechanisms between soil and structure in the liquefiable ground is very clear, but it still requires expensive computational efforts. Hence, the demand is always high for using the Beam-on-Winkler

Foundation method by modelling the soil surrounding the pile as disjointed springs and dashpots and solving the partial differential equations using the finite element or finite difference solutions [12].

1D modelling of the soil-pile system in liquefiable grounds is covered by (i) pseudo-static approach incorporating nonlinear p-y curve ([13], [14]), (ii) dynamic beam on Winkler foundation with pore pressure -dependent-stiffness and strength of the soil (e.g. [15]), (iii) macro-element approach using a mechanical representation of soil by spring-dashpot and gap model ([16], [17] and [18]).

One of the simple and reliable techniques for simulation soil-pile interaction in the liquefiable ground can be obtained by pseudo-static approach and inverted s-shape of the p-y curve [19],[20]. The inverted s-shape of the p-y curve was observed in field tests ([21], [22]), numerical plane strain [23], and T-bar tests ([24], [25], [26], [27],[28]) based on plane strain idealization of the soil-pile system at a particular depth to measure drag force on pile due to pulling a pipe in liquefied soil. [28] also reported that the dilative stiffening of the soil surrounding the pile increases the lateral soil resistance for higher loading rates and denser soil samples.

The pore pressures near the pile are affected by the strains produced by relative movements between the soil and pile, as shown by the tests at Treasure Island [21], 1-g shaking table test [29], 1-g T-bar tests ([26], [27], [28]), and dynamic centrifuge study [30]. However, [31] compared EPWP ratios measured in the near field and far field during the centrifuge study and found that the near-field EPWP were closely related to the far-field EPWP, with the near-field effects having a clear, but not dominant, effect on the pore pressures [32]. Experimental observations in large shaking table tests in Japan carried out by [33] also showed that the EPWP ratio is higher between the pile group comparing with far-field. Available simplified

1D models are failed to consider the additional effects of pore water pressure generation around the pile due to the dynamics of the pile.

Another shortcoming of existing 1D models is the sensitivity of the soil resistance to the relative velocity of the pile or additional soil strain rate effects which is the so-called 'dynamics of the system'. Experimental observations carried out by [27] and [28] showed that a large lateral resistance is provided as the loading rate increases ([27], [28]). This is opposed to the dynamic centrifuge study carried out by [31]. This can be considered by radiation damping [18].

While the soil-pile system should be modelled by the conventional hyperbolic shape of the p-y cure at the beginning of the earthquake, it must be transitioned into an inverted s-shape in the fully liquefied ground. Taking into account the effects of pile velocity or additional strain rate of soil as well as the difference between pore water pressure around the pile and the far-field, 1D modelling of the soil-pile system in the liquefiable ground is very complicated and is not addressed fully by available methods.

This study is aimed at developing a 1D model to be only tuned by soil properties and capturing the complex mechanism of soil-pile interaction to obtain the more accurate response of superstructure and substructure. This study will have several applications in geotechnical earthquake engineering as well as geotechnical engineering. The main benefit is reducing the computational time and cost of the analysis while the accuracy maintains high - suitable for several applications such as resilience-based assessment, performance-based assessment and seismic fragility analysis [34].

2. Physics of the soil behaviour around the pile

Previous research shows that the soil resistance decreases significantly underexposing cyclic loads on pile segments in the liquefied ground. That was illustrated by the results of T-bar tests ([23], [26], [29] and [27]), indicating that pile displacements under cyclic loading increase with several cycles and it is also thought that it will become larger than the displacements under monotonic loading in the non-liquefiable ground.

Shearing is explained by the distortional loading on soil elements. When a pile segment moves, it applies shear on the soil element and it induces this type of loading on soil additional to the shearing caused by the compression/extension mechanism [35]. Hence there will be a specific area to represent mobilised shear stress and shear strain. This area transfers the shear between the layers. Let us call the shear force on the surface of the soil around the pile segment i th by $V_{s,i}$. This can be explained as following:

$$V_{s,i} = \int\int \tau_i \, dA \qquad 1$$

where, τ_i is the resultant of all shear stresses in the direction of shear force. This equation can also be represented as follows:

$$V_{s,i} = \tau_{mob} \, A_{eq} \qquad 2$$

where, τ_{mob} is the mobilised shear stress on the surface of loading, and A_{eq} is the equivalent area of the surface mobilized by τ_{mob}. Owing to the elasticity of the soil, the mobilised shear stress may be presented by the shear modulus of the soil (G_s) and the mobilised shear strain ($\gamma_{s,mob}$) as shown by the author [35] in the past. As a result, it is postulated that a Representative Surface Element (RSE) and generally a Representative Volume Element (RVE) can be specified around the pile in which stress and strain will be uniform or homogenized. To explain the range of effective area around the pile affected by the mobilised shear stress and shear strain, a parametric analysis was carried out for flexible piles embedded in homogeneous-elastic strata [36].

To evaluate the mechanism of shear resistance in macro-scale, Figure 1 shows a schematic view of the pile and the two-dimensional set of circular particles initially in its densest possible packing. The shearing of the pile causes the particles located around the pile segment in each row to move sideways over the particles in the row below. Therefore, the particles fall into the gaps between other particles and the volume occupied by the soil reduces. On the other hand, as the particles in one layer are displaced sideways they are forced to climb over the particles in the underlying row and the volume occupied by the soil increases. These volume contractions and dilations are not uniform in the volume of the soil around the pile. This can be noted that its effect decays with radial distance from the pile centre. The mechanism similar to what appeared in the shear box test is localized around the pile. Depending on the relative density of the soil around the pile, volume contraction or dilation would be observed in RVE or RSE. Subsequently, the shearing of the pile may be followed by dilative (having peak value) or contractive behaviour of soil resistance.

Most of the deformation of the soil occurs in a thin zone around the pile interface. Hence there will be anisotropic volumetric and distortional strains around the pile, and these anisotropic strains change by distance from the pile. A schematic of this phenomenon is shown in Figure 2.

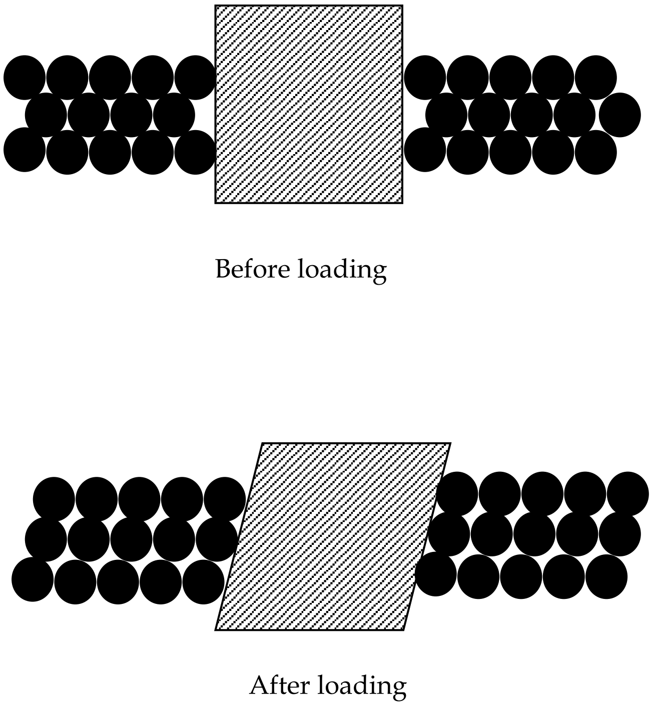

Figure 1. Mechanism of shearing soil resistance in micro-scale.

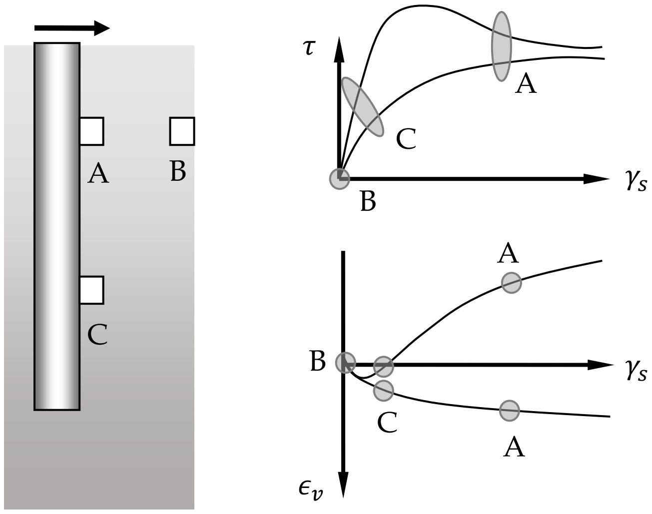

Figure 2. Effects of pile movement on distortional behaviour of the soil elements.

The compression/extension mechanism of soil resistance is computed by the movement of a rigid disk in a plane-strain section. This mechanism is subsequently resulting in the shearing mechanism localized around the pile segment. Hence the compression/extension mechanism is quantified by both in-plane shearing and compression/extension of the soil. On the other hand, the compression/extension mechanism of soil resistance causes the development of shear stress and strain on the shearing surface. Therefore, the mechanism of soil resistance should be represented by a generalized shearing resistance applicable to both individual compression/extension and shearing parts, as shown in Figure 3. These shearing mechanisms will result in the upward movement of soil located in front of the pile at a shallow depth layer.

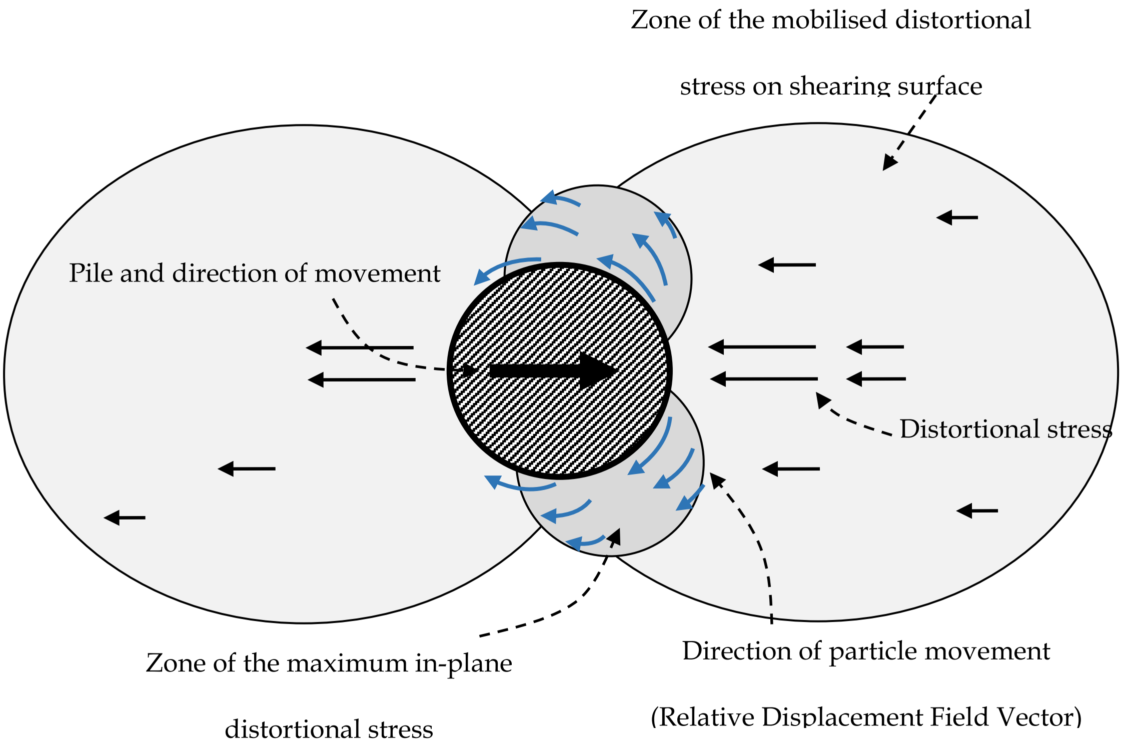

Figure 3. Shearing mechanism developed in soil by the lateral movement of a pile [36]

3. Macro-element model

3.1. Definitions and hypothesises

The pile response is mainly influenced by the response of soil located on a unit volume in the pile vicinity. The unit volume or RVE can be replaced by an element called '*macro-element*' which is much larger than soil elements defined in macro-mechanics. As a result, the link between the resistances and displacements is governed by macro-element constitutive relation.

Macro-element may compress/swell or distort as shown graphically in Figure 3. It shows a block of macro-element subjected to the shear stress so that it distorts in shear. As explained before, compression and distortion of RVE may occur during the lateral pile loading. This simple macro-element fails when no more resistance can be added and then it continues the displacement at constant resistance (p_y); this is defined as the strength resistance of the macro-element.

The stiffness and the strength are two important parameters of a macro-element as similar to constitutive behaviours of soil on the macro scale. The simplest theory for stiffness is attributed to the theory of elasticity, in which E_s and ν_s are kept constant during loading and unloading. The strength (p_y) is the limiting resistance that the macro-element can sustain as it suffers the large displacement. Owing to the categories of material behaviour in cohesive or frictional, limiting resistance may be calculated by one of the following forms:

(a) For cohesive material, it will be in the form of the following ([37], [38]):

$$p_y = \delta_u S_u D_p \tag{3}$$

where, S_u is soil undrained shear strength. δ_u is a factor that will be discussed here later (Section 4.3). D_p is the pile diameter.

(b) For frictional materials, it will be in the following form [39]:

$$p_y = \delta_u \sigma_v' \mu D_p \tag{4}$$

where, μ is the coefficient of friction. σ_v' is vertical effective stress.

The above stiffness and strength parameters may vary depending on soil types and loading conditions, so it makes the macro-element behaviour so complicated. On the other hand, strength may be a function of the rate of applied displacement (pile velocity). In this case, the viscous component of the macro-element will take the portions of total resistance.

Another parameter that will influence macro-element behaviour is the volumetric constraints of frictional materials around the pile. This should be considered by constitutive relation of macro-element. Hence the constitutive relation will consider both frictional and volumetric constraints.

When the macro-element fails, distinct slip surfaces of soil develop around the pile. Slip surfaces separate blocks of soil and consequently yields the non-relative movements of soil blocks. This theory is mainly applicable for the failure of the pile loaded by dynamic or static pile-head loading at ground level (see for example Figure 4) and it is not subjected in this research.

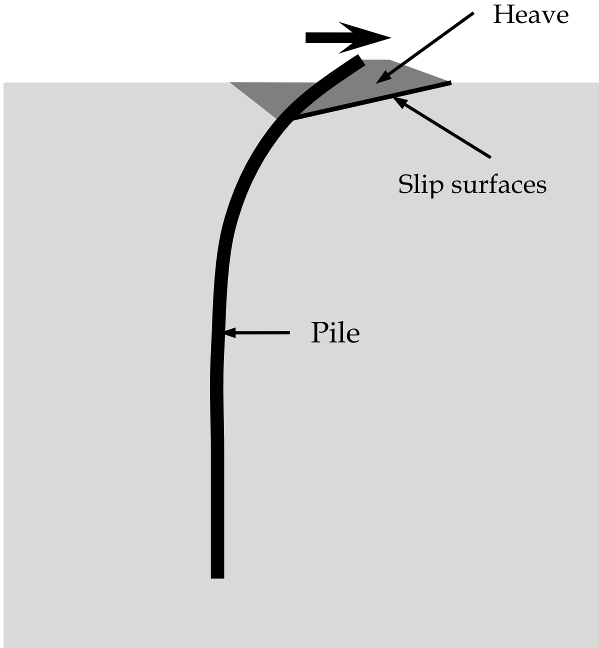

Figure 4. Slip surface developed in soils surrounding the pile loaded at the pile head.

3.2. Formulae

3.2.1. Basic Concept

For frictional materials, stress ratio is more important than shear stress at the macro scale, hence Eq. 4 would be represented by resistance ratio as follows:

$$\frac{p_y}{S} = \eta_y = \delta_u \mu \tag{5}$$

where, $S = \sigma_v' D_p$ is named as *average-effective resistance* of soil in macro-element. This is very similar to a part used by [17], in which the average effective stress ratio can be obtained by the average effective stress (σ_v') and the pile diameter. This resistance ratio (p_y/S) is clearly specified by two resistance parameters: (a) p which is lateral resistance of macro-elements (force per unit length exerted by macro-element), and (b) S which is average-effective resistance of macro-element. Hence, it is presumed that the macro-element behaviour is influenced by both $p - S$ space and $p - y$ space, in which, S will consider effects of the effective soil resistance on soil-pile interface of macro-element. This effect will be prominent in the undrained loading condition of the sand-pile system. In this case, a point of resistance is moving on a path called '*resistance path*', comparable to the stress path in macro-mechanical constitutive models.

Based on the simple Mohr-Coulomb failure criterion, the resistance surface is assumed to be a cone shape. As a result, the $p - S$ space may be schematically exhibited in Figure 5. To make a robust analysis and coherency with macro-scale constitutive relation, the bounding surface plasticity is developed to locate the image resistance.

The nonlinearity of macro-element in frictional material is coupled with its volumetric behaviour and both effects may not be separated from each other. However, the simple p-y curves usually can't deal with it. To consider volumetric constraint into the macro-element formulation, the dilatancy surface is added to $p - S$ space. As shown in Figure 5, the bounding surface and the dilatancy surface are two important ingredients for simulating the dilative behaviour of macro-elements and the hardening rule.

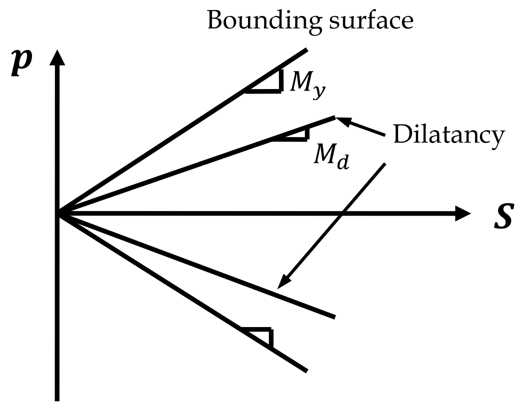

Figure 5. p-S space in the Macro-element.

3.2.2. Frictional constraint

Using the Mohr-Coulomb failure criterion, Eq. 5 is rewritten as follows:

$$\frac{p_y}{S} = M_y \qquad 6$$

where, M_y is so-called *limiting resistance ratio* or *bounding resistance ratio*. Unlike the triaxial compression and extension, the same limiting resistance ratio is applied on the macro-element for compression and extension sides. This rule can be changed if two piles are located close to each other. In this case, a proper investigation should be done which is out of the aims of this research.

3.2.3. Volumetric constraint

The classical theory of the p-y curve ensures that p (the force per unit length exerted by a spring) and y are linked by K_s which is shearing and compression/extension stiffness of the soil-pile system [35]. This simple relation may not be used for soil-pile system in the liquefiable and laterally spreading ground (e.g. [13], [14], [40]). Hence another robust theory would be used here to consider the variation of effective soil resistance and volumetric constraint involved in such a complex phenomenon.

According to the above theory of macro-elements, the constitutive equations of the macro-element will be written in terms of the resistance and displacement parameters. Houlsby [41] postulated that the dilation, which occurred at the soil–pile interfaces (for frictional materials), is the primary mechanism responsible for the large shaft resistance observed in small diameter piles. It is worth mentioning that the cavity expansion theory ensures that radial compression/extension of the soil around a cavity can be linked to normal effective stress ($d\sigma_n = K.dv$, in which K is stiffness and v is radial compression/extension). To consider this effect into the macro-element which will be influenced by lateral movement of the pile, it postulates from the cavity expansion theory in which a relation exists between average-effective resistance of soil (S as explained above) and the radial contraction/expansion of the soil-pile interface (v). Radial contraction/expansion is a so-called volumetric constraint here later. This expression is provided as following for elastic soil:

$$S = \mathrm{N}v \tag{7}$$

where N is the stiffness linking average-effective resistance and the volumetric constraint. This may also be called volumetric stiffness of the soil-pile system. This concept is similar to the bulk modulus linking the volumetric strain and the mean effective stress, in macro-scale geotechnics.

N is supposed to be a material constant. As an initial conjecture, it may also be defined in cavity expansion theory as given by [42]:

$$\mathrm{N} = \Upsilon G_{max}\left(\frac{\sigma_v'}{\sigma_n'}\right) \tag{8}$$

where, G_{max} is the maximum elastic shear modulus of soil surrounding the pile segment at small strain levels (the amplitude less than 0.0001 %). σ_n' is the effective normal stress applied on a soil-pile interface. [42] estimated that Υ varies in the range of 0.03 to 0.15 for non-displacement piles in sand.

The maximum elastic shear modulus of sand (G_{max}) may also be calculated by following general form [43]:

$$G_{max} = G_0 F_{(\vartheta)} p'^n \qquad 9$$

where, G_0 and n are material parameters ($n = 0.5$ for sand), ϑ is the specific volume, p' is the mean effective stress. $F_{(\vartheta)}$ is a function considering specific volume or void ratio of sand and it varies depending on the roundness of grains. In a level ground condition, $p' = (1 + 2K_0)\sigma'_v/3$, where σ'_v is the effective vertical stress and K_0 is the lateral earth pressure coefficient at rest.

3.3. Constitutive relation of macro-element

3.3.1. Elastic formulation

Following the above description of the macro-element resistances and displacements components, the hypoelastic constitutive relation of the macro-element is to link resistance vector ($\{p \quad S\}^T$) and displacement vector ($\{y \quad v\}^T$) by isotropic hypoelasticity (D^e) as following:

$$\begin{Bmatrix} dp \\ dS \end{Bmatrix} = [D^e] \begin{Bmatrix} dy^e \\ dv^e \end{Bmatrix} \qquad 10$$

where,

$$[D^e] = \begin{bmatrix} K_s & 0 \\ 0 & \mathrm{N} \end{bmatrix} \qquad 11$$

According to an elastic assumption for the macro-element, uncoupled relation between soil lateral resistance (p) and volumetric constraint (v) of the macro-element is postulated. In the case of the nonlinearity of the macro-element, coupling effects are taking into account by influencing the lateral resistance by volumetric constraint and average-effective resistance by lateral-relative pile displacement. Following this concept, slippage on the soil-pile interface may be developed by history-dependent material behaviour and residual resistance. This means that slippage is developed by some residual effective or lateral resistances which will be explained later.

Since volumetric constraint on the soil-pile interface is negligible, it is assumed here that v is defined as the induced volumetric constraint by far-field motion. This means that $dv = 0$ for laterally loaded piles and $dv \approx dS_{ff}$ for earthquake-induced vibration of the soil-pile system. $dS_{ff} = D_p \sigma'_{v,ff}$ expresses the variations of average effective stress in far-field ($\sigma'_{v,ff}$). Since we are dealing with average-effective stress/resistance, drained and undrained condition is separated by a simple assumption related to the variation of S. It is postulated that $dS = 0$ for drained condition, this provides simple p-y curved as already proposed in the literature.

Schematic of the $p - S$ space and $p - y$ space for laterally loaded pile segment in the undrained condition is shown in Figure 6. As it can be observed, slippage of soil surrounding the pile develops by vanishing the vertical resistance of the macro-element.

For saturated deposits induced by earthquake loading and subsequently liquefaction of the ground, the time required for drainage is 10 to 30 min for a sand deposit having several meters thickness [44]. The effective time duration of an earthquake is 10 to 20 sec. Hence it is realistic to assume fully undrained conditions for a soil-pile system in the liquefiable ground. As a result, slippage is likely to develop on the soil-pile interface.

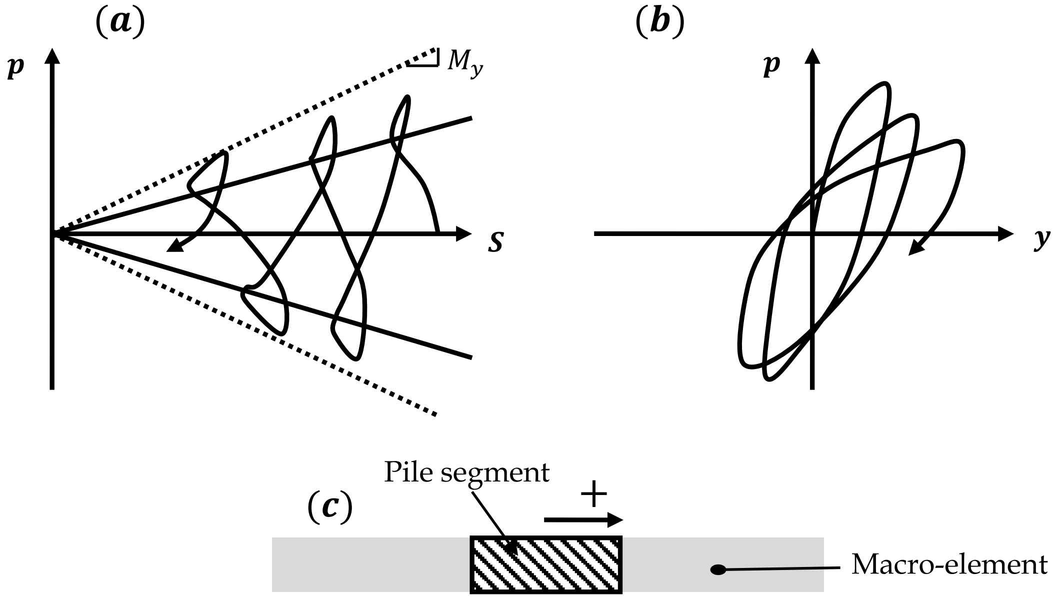

Figure 6. Schematic view of the Macro-element behaviour in undrained loading condition; (a) p-S space, (b) p-y space, and (c) convention of loading

3.3.2. Flow rule

To consider effects of (1) building up pore pressure on soil-pile interface, (2) slippage on soil-pile interface due to earthquake loading, and (3) mechanism of energy dissipation on the pile and the macro-element responses, it may be necessary to assume a flow rule for the macro-element similar to which is usually developed in macro-scale constitutive models.

Incremental plastic work done in the macro-element may be obtained as follows:

$$dW = p\,dy^p + S\,dv^p \qquad 12$$

As mentioned before, a macro-element is influenced by both compression/extensions loading and distortional loading. To simplify the mechanism of the energy dissipation in the macro-element, it is assumed that the above incremental plastic work is entirely dissipated in friction at all stages of a pile movement. This assumption is initially assumed by Taylor [45] in macro-scale of frictional materials and then elaborated by some refinement over the angle of resistance (dilation) in the vast body of works of literature. By this context, Eq. 12 is re-casted as follows:

$$p\,dy^p + S\,dv^p = M^d\,S\,dy^p \tag{13}$$

where, $M_d = \lambda_d M_y$ is the resistance ratio which dilatational behaviour of the macro-element is introduced, it is also referred to as the dilatancy surface of macro-element in $p - S$ space. λ_d is a factor indicating the dilatancy surface as a fraction of the limiting resistance surface. It is also similar to the concept used by [17]. To use the above equation as a flow-rule of the macro-element, the following equation is presented:

$$d = \frac{dy^p}{dv^p} = A_0 A_c A_s\left(M^d - \eta\right) \tag{14}$$

where, η is the resistance ratio as $\eta = p/S$. A_0 is a material parameter, controlling the intensity of dilatancy. A_s is a parameter considering the effects of unloading on the macro-elements flow rule. A_c is the parameter considering the effects of accumulated volumetric constraint in the dilation phase on the compression phase.

To consider the effects of unloading on the shape of resistance-dilatancy relation, an auxiliary concept is investigated here as follows:

$$A_s = \frac{1}{\sqrt[2]{\dfrac{1 + (M^d - \eta)^2}{\eta - \eta_u}}} \tag{15}$$

where, η_u is the resistance ratio of the unloading resistance point.

The effect of the accumulated volumetric constraint on the compression part of the resistance-dilatancy equation is investigated by A_c as follows:

$$A_c = \begin{cases} 1 + \chi.\xi_v & if \quad dS < 0 \\ 1 & if \quad dS \geq 0 \end{cases} \tag{16}$$

where, χ is a model parameter controlling the rate of the developing pore-water pressure around the pile. ξ_v is the accumulated volumetric constraint in the dilation phase. It is calculated by the following equation:

$$\xi_v = \begin{cases} 0 & if \quad dS < 0 \\ \int \frac{dS}{\mathrm{N}} & if \quad dS \geq 0 \end{cases} \tag{17}$$

To consider flow rule into elastoplastic relation, the direction of the plastic flow (m) is defined as the following:

$$m = \begin{Bmatrix} 1 \\ d \end{Bmatrix} \tag{18}$$

3.3.3. Hardening rule

It is assumed that the plastic-relative displacement of pile is a function of resistance ratio (η) developed in the macro-element. Following the classical hyperbolic equation [46], the plastic modulus is defined as:

$$H_s = \frac{b^2}{b_{max}B} \tag{19}$$

where, b is the distance between the current resistance ratio and the bounding resistance ratio ($b = M_y - t.\eta$). b_{max} is the maximum possible value of b when the current resistance surface is close to the bounding resistance surface. On the other hand, the effects of unloading (η_u) should be considered, hence it will be $b_{max} = \left(M_y - t.\eta_u\right)$. t is auxiliary parameter taking +1 if $dy \geq 0$, and -1 if $dy < 0$ (see for example Figure 7). B is defined as the value assigning the rate of displacement development. To consider effects of degradation of the macro-element by the accumulated plastic-relative displacement of the pile, the following relation that interpolates the B value is proposed (based on the similar concept in macro-scale geotechnics by [47]) as:

$$\frac{1}{B} = \left(\frac{1}{B_{min}} - \frac{1}{B_{max}}\right) \exp\left(\frac{-\xi}{y_{c0}}\right) + \frac{1}{B_{max}} \tag{20}$$

where, B_{min} and B_{max} are material parameters as the minimum and maximum attainable B value, ξ is accumulated plastic-relative displacement of the pile ($\xi = \int dy^p$), and y_{c0} is a material parameter as plastic-relative displacement of the pile at which $B = B_{max}$. Initial evaluations show that variations of B value have not significant effects on the macro-element response, hence B_{min} can be equal to B_{max}.

Owing to the presented hardening rule, plastic-relative displacement of pile is calculated by:

$$dy^p = \frac{d\eta}{H_s} \tag{21}$$

The above equation may also be rewritten as follows:

$$dy^p = \frac{d\eta}{SH_s}\begin{Bmatrix} 1 \\ -\eta \end{Bmatrix}^T \begin{Bmatrix} dp \\ dS \end{Bmatrix} \tag{22}$$

where, n^T is the transpose of the loading direction vector.

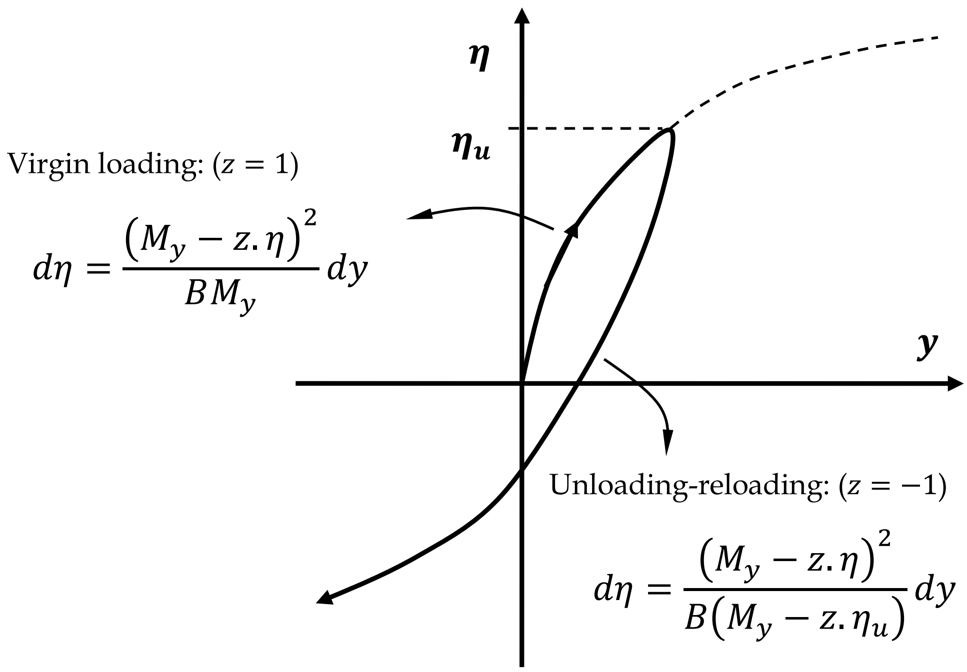

Figure 7. Schematic of hardening modulus in drained cyclic loading

3.3.4. Elasto-Plastic formulation

Following the initial principles in plasticity and the hypoelastic formulation, resistance-displacement relation is defined as:

$$\begin{Bmatrix} dp \\ dS \end{Bmatrix} = [D^{ep}] \begin{Bmatrix} dy \\ dv \end{Bmatrix} \tag{23}$$

where,

$$[D^{ep}] = \left[D^e - \frac{D^e m n^T D^e}{SH_s + n^T D^e m}\right] \tag{24}$$

The tangent stiffness (D^{ep}) may also be introduced by the following expression:

$$[D^{ep}] = \begin{bmatrix} K_s - \dfrac{K_s^2}{SH_s + K_s - \mathrm{N}\eta d} & \dfrac{K_s \mathrm{N}\eta}{SH_s + K_s - \mathrm{N}\eta d} \\ \dfrac{-K_s \mathrm{N}d}{SH_s + K_s - \mathrm{N}\eta d} & N + \dfrac{\eta \mathrm{N}^2 d}{SH_s + K_s - \mathrm{N}\eta d} \end{bmatrix} \tag{25}$$

For the soil-pile system induced by pile-head loading in undrained condition, it is expected that the lateral soil resistance of the macro-element will be limited by some value. This concept will be important if $p - S$ path goes towards the bounding surface line. As there is the following equation for monotonic undrained loading:

$$dp = \frac{K_s(SH_s - \mathrm{N}\eta d)}{SH_s + K_s - \mathrm{N}\eta d} dy \xrightarrow{H_s \to 0} dp = \frac{-K_s \mathrm{N}\eta d}{K_s - \mathrm{N}\eta d} dy \tag{26}$$

and $H_s \to 0$ on the bounding surface, $p - y$ curve will pass towards lines such as AB or A′B′, as shown in Figure 8.

If we ignore any limitations associated with the vertical soil resistance (as mentioned by S_c in Figure 8), the macro-element will be failed to capture the soil-particle crushing around the pile which would be expected to happen in a large deformation mechanism. This has resulted in a limiting soil resistance (after point B and B' in Figure 8). For sake of brevity, the crushing particles and large strain mechanism of the granular material is excluded in this research.

Figure 8 also shows the shape of two types of $p - y$ curves that are served in the literature as hyperbolic curves before the earthquake and inverted s-shape during cyclic mobility ([14][13],[20]). These would be well-simulated by the macro-element concept in this research.

For drained condition ($dS = 0$), $p - y$ relation (Eq. 23) can be summarized as the following relation:

$$dp = K_s\, SH_s \left(1 - \frac{\mathrm{N}\eta d}{SH_s + K_s}\right) dy \qquad 27$$

This equation shows that the effects of flow rule (d) and elastic volumetric stiffness (N) would be negligible in drained condition as $K_s\, SH_s$ already controls the $p-y$ relation. Large strain mechanism and particle crushing will be more effective in the drained condition which is ignored in this study.

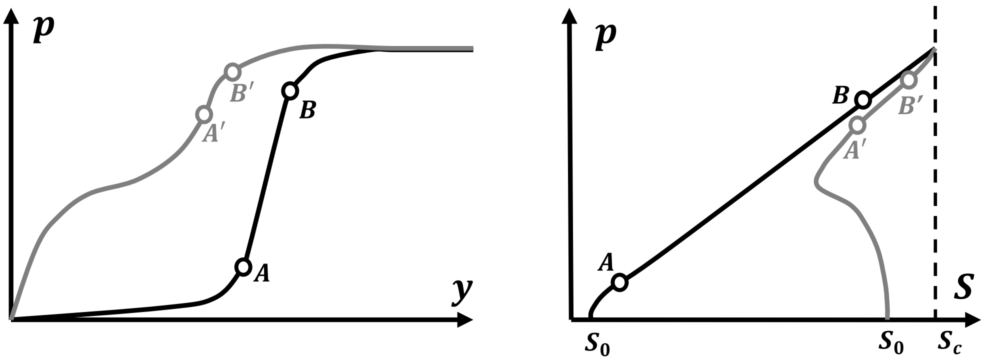

Figure 8. p-S space and p-y space for two cases of initial condition under one-way lateral loading in undrained condition.

3.3.5. Residual resistance

The minimum attainable resistance sustained by the soil surrounding the pile is called the residual resistance. The residual resistance is used in the lateral spreading design concept in the force-based method (i.e. [48]). This minimum resistance is observed when the slippage appears on the soil-pile interface or the soil is fully liquefied and laterally flows. To consider this effect into macro-element, the minimum average-effective resistance of soil (S_{min}) is assumed and subsequently the minimum force per unit length of the pile exerted by macro-element (p_{min}) will be proportional to it. To avoid numerical difficulties at fully liquefied soil surrounding the pile which yields to the slippage of the soil-pile interface, a small positive value is assigned to S_{min}. In this case, zero dilatancy emerges for the domain where the resistance path is on the minimum soil resistance. The dilative phase appears by intersecting the resistance path with the dilatancy surface. The schematic of this phenomenon is shown in Figure 9. In this concept, p_{min} is calculated as following:

$$p_{min} = M_d S_{min} = \lambda_d M_y S_{min} \quad 28$$

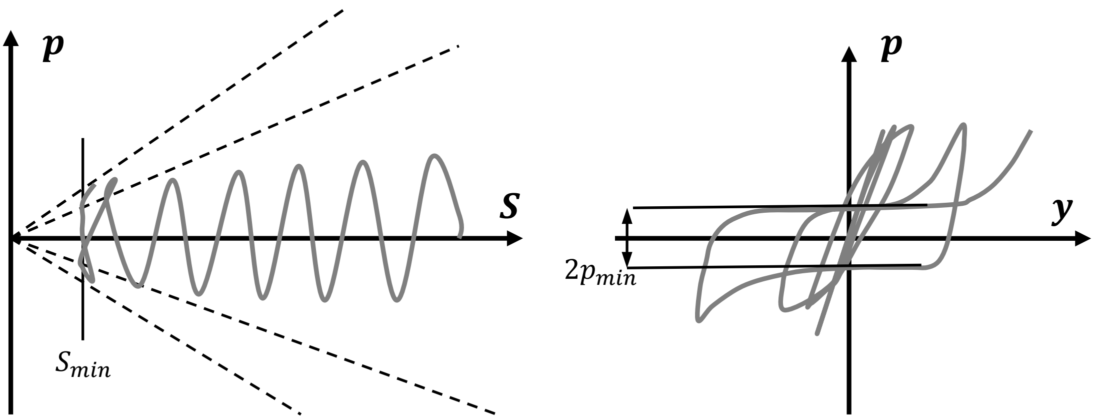

Figure 9. The schematic of effects of residual resistance.

3.4. Effects of Dynamics (Modelling radiation damping)

As extensively explained by [49], the geometric damping or the radiation damping of the soil-pile system must be considered in the calculation in design procedure when the dimensionless frequency of loading is greater than a limited value, so-called radiation dimensionless frequency. Due to the elasticity of soil, $p - y$ relation can be rewritten as following:

$$p = K_s y + D_c \dot{y} \quad 29$$

where, D_c is the damping and $\dot{y}$ is the pile relative velocity. In this basic equation, the dashpot is launched parallel to the spring (Kelvin-Voigt model). The above equation can also be cast as follows:

$$dp = D^{ep}_{(1,1)} dy + D^{ep}_{(1,2)} dv + D_c \, d\dot{y} \quad 30$$

Please note that the above visco-elasto-plasticity has a different form of visco-plasticity defined by the Bingham model and overstress's theorem [50]. The soil horizontal resistance is given by three terms; (1) classical $p-y$ term ($dp_s = D^{ep}_{(1,1)}dy$), (2) the dashpot component ($dp_d = D_c\, d\dot{y}$), and (3) the term related to the effect of the induced volumetric constraint of the macro-element on soil resistance ($dp_v = D^{ep}_{(1,2)}dv$). dp_v might also be zero for laterally loaded piles or may be defined by some equations/assumptions to simulate the partial liquefaction or drainage of pores.

The plastic radiation damping is also considered into the dashpot component similar to the hardening rule adapted for stiffness component, by the following equation:

$$D_c = \frac{C_r}{2}\left(1-\frac{\eta}{M_y}\right)^2 \tag{31}$$

for a simple representation, or

$$D_c = \left(\frac{D_s^{ep}}{K_s}\right)C_r \tag{32}$$

for complex one. D_s^{ep}, which makes a direct link between dp and dy, is obtained by Eq. 26 for fully undrained conditions and Eq. 27 for fully drained conditions. C_r is the quasi-elastic radiation damping which is calculated by [49]:

$$\frac{C_r}{D_p\rho_s V_s} = 4.1a_0^{-1/5}\left(1+\frac{V_c}{V_s}\right)(1.186\exp(-0.777\delta_s) - 0.186\exp(-5.71\delta_s)) \tag{33}$$

Where, δ_s is the hysteretic damping of soil material, V_c is the wave velocity represented for radiation damping, $V_s = \sqrt{G_{max}/\rho_s}$ is the shear wave velocity of the soil. ρ_s is the saturate mass density of the soil. More explanations would be found in the original research of the authors.

The concept of considering this type of radiation damping is called '*stiffness-proportional nonlinear damping*' ([51], [52], and [17]). Because it is a function of resistance ratio, Eq. 31 overestimates the radiation damping when slippage develops on the soil-pile interface, specifically when $S = S_{min}$. It is expected that the transfer of vibration energy from pile to soil becomes negligible when slippage develops on soil-pile interface, but Eq. 31 presents some radiation damping and provides sensitivity of soil resistance to pile velocity. This condition will not be exhibited by Eq. 32.

The main features of the presented visco-elasto-plasticity (Eq. 30 and 32) are: (1) the dynamic stiffness is the stiffness proportional, and (2) the differentiation of horizontal soil resistance (dp) is a function of stiffness-proportional term (D_s^{ep}/K_s), and this makes a stable-numerical solution.

4. Calibration of the macro-element

To simulate the macro-element behaviour in FEM, material parameters need to be calibrated. They would be defined by initial geotechnical investigations, empirical equations or engineering judgments. Table 1 shows the list of model parameters in this study. They are categorized into six sections covering elasticity, limiting resistance, hardening modulus, flow rule, residual resistance and radiation damping. The latest one has already been explained above as well as in [49] so other parameters are discussed in this section.

4.1. Shearing Stiffness (K_s)

Shearing elastic stiffness is the basic stiffness component of soil-pile systems which is usually presented by a stiffness factor (α) times the elastic Young's modulus of soil surrounding the pile (E_s). The stiffness factor can be obtained by the concept developed by the author [49] and [35]. The stiffness factor considers the effects of the relative displacement of the pile and pile curvature. In the case of true plane strain, α may vary from 1 to 2.5 for wide ranges of elastic-modulus ratio (E_p/E_s) and pile head condition, as shown by the author for homogeneous soil [49]. In the case of soil inhomogeneity, assigning α may need more effort. The following steps propose a routine for assigning best α value for the pile embedded in inhomogeneous soil and loaded by some sort of dynamic loading conditions:

Step 1: model soil-pile-superstructure system by continuum approach, presented by [49].

Step 2: Calculate the predominant period of the soil-pile-superstructure system by applying unit loading but different frequencies on superstructure level, and measuring displacement.

Step 3: Simulate the macro-element approach (by assuming elastic soil condition) by different α value and measure the predominant period of the system due to soil elasticity.

Step 4: Select best α for the case in which the continuum solution and the macro-element approach have the same predominant period.

Table 1. Model parameters in the 1D macro-element

Category	Model Parameters	Equations
Elastic (K_s, N)	α, $_0$, N †	$K_s = \alpha\ E_s$ $E_s = 2\ G_s\ (1 + \nu_s)$ $G_s = \ _0 . F_{(\vartheta)} . (p'^{0.5})$ $\vartheta = 1 + e$ ‡
Limiting Resistance (M_y)	ϕ*	Broms (1964): $M_y = 3K_p$** Barton (1982): $M_y = K_p^2$ Varun et al (2013): $M_y = 3.25K_p + 0.3\ K_p^2$
Hardening rule (B)	B_{min}, B_{max}, y_{c0}	$\frac{1}{B} = \left(\frac{1}{B_{min}} - \frac{1}{B_{max}}\right) exp\left(-\frac{\xi}{y_{c0}}\right) + \frac{1}{B_{max}}$
Flow rule (d)	A_0, χ, λ_d	$d = A_0 . A_s . A_c . A_d (M_d - \eta)$ $A_c = 1 + \chi\xi_v$ $M_d = \lambda_d M_y$
Residual resistance (p_{min})	S_{min}	$p_{min} = \lambda_d M_y S_{min}$
Radiation damping	C_r	

† $_0$ is the material parameter.
‡ e is the void ratio of soil.
* ϕ is the friction angle of soil.
** K_p is passive earth pressure defined as $K_p = \frac{1+\sin(\phi)}{1-\sin(\phi)}$.

Elastic Young's modulus of soil surrounding the pile (E_s) may also be calculated by shear modulus (Eq. 19) and Poisson's ratio of soil. Shear Modulus (Eq. 19) needs the model parameter G_0 which may also be defined by the method presented in the vast body of literature. It defines the elastic shear modulus of sand and it can be calibrated using the elastic wave propagation tests by seismic methods or the stress-strain curves in the field or laboratory.

4.2. Volumetric Stiffness (N)

As explained in the previous section, the volumetric stiffness is proposed to link the variation of the vertical soil resistance (S) and the volumetric constraint (v) in the elasticity. This parameter was proposed for axially loaded non-displacement piles to evaluate its settlement, and it was defined to be a function of the maximum shear modulus of soil. In this study, the volumetric stiffness is suggested to be a function of elastic shear modulus (G_{max}) as following:

$$\mathrm{N} = \Upsilon G_{max} \qquad 34$$

where ϒ is given by different values (i.e 0.008 would be first trying) (see for example; [42] for axially loaded non-displacement piles). There is an element of compromise in its selection.

4.3. Limiting resistance

[53] suggested the limiting resistance ratio given by:

$$M_y = 3K_p \qquad 35$$

where, K_p is the passive earth pressure. However, the comparisons with field test results show a tendency for the measured resistance ratio to be underestimated by about 30% using the above expression ([54], [55]). [39] also proposed limiting resistance ratio which varies from K_p at top and then becomes K_p^3 in higher depth.

Another method for predicting the limiting resistance ratio for sand is presented by [38]. The initial slope of the p-y curves and the shape of the curves are the main differences of [38] and [39].

[56] proposed the following limiting resistance ratio after comparing with the field test data as:

$$M_y = K_p^2 \tag{36}$$

Another equation was presented by [17], after comparing with the results of the FE model, as following:

$$M_y = 3.25K_p + 0.3K_p^2 \tag{37}$$

The above relation is used in this study. The passive earth pressure in all the above equations is obtained as follows:

$$K_p = \frac{1 + \sin\phi}{1 - \sin\phi} \tag{38}$$

where ϕ is the friction angle of the soil. Triaxial compression tests are recommended for obtaining the friction angle of the sand. On the other hand, the effective friction angle of sand may also be calculated by SPT N-value (i.e. [57]) or CPT test results (i.e. [58]).

4.4. Hardening modulus

Hardening modulus (B) is defined by three parameters; B_{min}, B_{max}, and y_{c0} or can be stand-alone by a B_{min} value. Theoretically, B_{min} would be calculated by elastic stiffness (K_s) in drained loading conditions as following:

$$B_{min} = \frac{S\,M_y}{K_s} = \frac{D_p \sigma_v' M_y}{K_s} \quad (39)$$

In this case, both the elastic stiffness (K_s) and B_{min} may vary with $\sqrt[2]{\sigma_v'}$. This equation overestimates the evolution of the plastic displacement of the pile (relative displacement). Hence adopting a constant value may be a better choice for the hypoelastic constitutive equation of the macro-element presented in this study.

For better evaluation, B_{min} can be equal to y_{50} where, y_{50} is the displacement mobilized by 50 per cent of the limiting lateral resistance (p_y).

To obtain B_{min}, B_{max}, and y_{c0}, p-y curves of drained loading conditions would be suggested. In such a case, API recommended that p-y curves can be alternatively used, and the material parameters are deduced through a trial-and-error procedure and also a global optimization procedure based on the Simplex method.

4.5. Flow Rule

The basis of the flow rule provided in the macro-element is equivalent to the flow rule in the Original Cam Clay model [59], in which dilatancy line or Phase transformation line [60] is introduced by dilatancy surface. The rate of the volumetric constraint of the macro-element is zero when the resistance path is posed on the dilatancy surface.

4.5.1. The slope of Dilatancy surface

The investigations in FE models carried out by [17] showed that the slope of dilatancy surface or the phase transformation line is independent of the pile diameter, depth where the pile segment is located, the friction angle, and the liquefaction resistance parameter. It was concluded that the slope of the phase transformation line is controlled by the critical state friction angle (ϕ_{cv}) and the following equation:

$$M_d = 3.25 \frac{1 + \sin\phi_{cv}}{1 - \sin\phi_{cv}} \tag{40}$$

To obtain the angle of dilation for sand, the following empirical formulation proposed by [61], the correlation between relative density (or maybe void ratio, in some empirical correlations) and the cone tip resistance (q_c) is the necessary ingredient (see for example [62]). Critical state friction angle of sand can also be obtained due to mineralogy (i.e. 33^0 for quartzitic sand and 40^0 for feldspathic sand).

4.5.2. Liquefaction resistance parameter (A and A_c)

Liquefaction resistance parameters A and A_c are the scaling parameters for both dilative and contractive phases, and contractive phases only, respectively. The parameter controlling the contractive phase only is χ of which its higher value yields to the higher rate of generation of excess-pore-water pressure, and consequently the quicker degradation of soil strength around the pile in each cycle. The role of A is very significant at the post-liquefaction stage when the dilative response is exhibited by macro-element. The higher A value, the stronger the dilative response at post-liquefaction.

The best-initial choice for A value can be A_0 which can be thought of as slope of stress-dilatancy line obtaining by laboratory experiments (drained loading condition). There is an element of compromise in its selection, as well, and it will be explained during some simulations here later.

4.6. Residual resistance

Like the macrostructure of sand, the macro-element is a pressure-dependent element. Hence both its modulus and the resistance depending on the current vertical soil resistance (average of vertical effective stress in the macro-element). To avoid numerical difficulties at fully liquefied soil surrounding the pile which yields to the slippage of the soil-pile interface, a small positive value is assigned to the vertical soil resistance, denoted as S_{min}. In this case, residual horizontal resistance of the macro-element may be simply calculated by Eq. 28. On the other hand, residual resistance can be calculated by some code of practice (e.g. [48]) which proposes this value for laterally spreading soil.

5. FEM

The main differences between the 1-D macro-element presented in the current research and nonlinear BWF are counted by (a) effects of variation of the vertical effective stress of soil surrounding the pile are considered in the macro-element but it is neglected in BWF which is based on p-y curves, (b) the volumetric constraint of the macro-element is also considered in current research. Unlike BWF which is a one-dimensional spring model, the macro-element is developed by an element that has two displacement components on each side and two soil resistances stored in it (Figure 10).

In this study, a Finite element model is developed to simulate realistic behaviour of soil surrounding the pile under dynamic or static loadings induced by pile-head or earthquake vibrations in sandy deposits. Macro-elements are mounted on the nodal points of the pile.

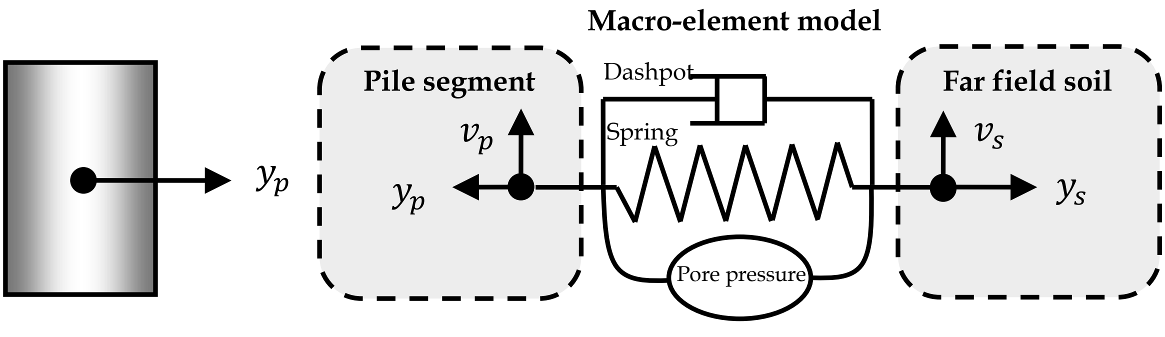

Figure 10. Schematic the 1-D macro-element model.

To compute the time-history response of a single pile, the global Mass ($[M]$), global Stiffness ($[K]$), global damping ($[C]$) matrices and global input forces ($[P_{(t)}]$) should be initially obtained. The second-order differential equation of a dynamic system and the linear system of the equation of a static system are as following:

$$\begin{cases}[M]\{\ddot{q}\} + [C]\{\dot{q}\} + [K]\{q\} = \{P_{(t)}\} \\ [K]\{q\} = \{P\}\end{cases} \tag{41}$$

Global mass, stiffness and damping matrices are assembled by local mass, stiffness, and damping matrices, respectively, obtained from beam element (for pile) and the macro-elements (for soil surrounding the pile). Displacement vector ($\{q\}$) is obtained as a particular solution adopted on the model using defined boundary conditions in each time step which are assigned manually and explained in numerical examples. The external force ($\{P_{(t)}\}$) is the part of known vectors in the system related to the induced loadings, or boundary conditions.

Obtaining the local mass, stiffness and damping matrices of beam elements are extensively used in the vast body of literature. In this study, the 2D beam element is used to model single-pile, and the damping matrix is calculated by Rayleigh damping formulation as follows:

$$[\bar{C}] = a_0[\bar{M}] + a_1[\bar{K}] \tag{42}$$

where, $[\bar{M}]$, $[\bar{K}]$, and $[\bar{C}]$ are local mass, stiffness and damping matrices of the beam element. a_0 and a_1 are Rayleigh damping coefficients of mass and stiffness, respectively. These scalar values (a_0 and a_1) are computed using two significant natural modes of i and j using the following expression [63]:

$$\begin{Bmatrix}\xi_i \\ \xi_j\end{Bmatrix} = \frac{1}{4\pi}\begin{bmatrix}1/f_i & f_i \\ 1/f_j & f_j\end{bmatrix}\begin{Bmatrix}a_0 \\ a_1\end{Bmatrix} \tag{43}$$

where, f_i and ξ_i are natural frequency and damping ratio in mode *i*.

Local stiffness ($\bar{K}_{me}$) and damping ($\bar{C}_{me}$) matrices of macro-elements are obtained by the output of the constitutive matrix as follows:

$$\bar{K}_{me} = \begin{bmatrix} D^{ep} & -D^{ep} \\ -D^{ep} & D^{ep} \end{bmatrix}_{4\times4} \tag{44}$$

and,

$$\bar{C}_{me} = \begin{bmatrix} D_c & 0 & -D_c & 0 \\ 0 & 0 & 0 & 0 \\ -D_c & 0 & D_c & 0 \\ 0 & 0 & 0 & 0 \end{bmatrix}_{4\times4} \tag{45}$$

where D^{eq} is obtained by Eq. 25, and D_c is calculated by Eq. 32.

The global boundary conditions applied to the system is as follows:

1. Pile-head restraint condition: depending on the fixity of the pile head, boundary conditions are applied.
2. Pile-tip restraint condition: pile is vertically restrained for neglecting pile settlement.
3. Far-field displacement, velocity and acceleration are linked to the far-field side of the macro-element.
4. The volumetric constraint of the far-field side of the macro-element (v_s) is calculated by variations of pore-water pressure generated in soil located at a far-field. The following equation is used to obtain variations of induced volumetric constraint:

   $$dv_s = \frac{dS_{ff}}{D^{ep}_{2,2}} \tag{46}$$

   where, $dS_{ff} = D_p \sigma'_{v,ff}$, and effect of pore-water pressure variations is directly considered into $\sigma'_{v,ff}$.

5. Because of assuming negligible void redistribution on the soil-pile interface during dynamic loading, the volumetric constraint of pile segment (v_p) is always kept zero.

For the system presented here of which the macro-element shows a nonlinear-dynamic behaviour (or nonlinear-static behaviour), the numerical time-stepping method for integration of differential equations in Boundary Value Problem (BVP) is used. A vast body of literature exists about the methods for solving various second-order differential equations (or linear systems of equations). Newmark algorithm [64], as the oldest and most extensively used algorithm for the integration of the equations of dynamic systems, is used in this study. To avoid accumulating errors in each additional load step, equilibrium iterations are used to establish equilibrium to the desired degree of accuracy at each load step using the Newton–Raphson method. This method has some inefficiencies for the systems where the stiffness changes rapidly, and in particular, around load limit points where the sign of the load increment changes downward. Hence some other techniques are proposed in the literature. In this study, the Newmark time-stepping technique is used by adopting a very small time step (i.e. 0.001 sec), as an original computing time-step, to enable simulating the softening exhibited by the macro-element. This might not be the computationally optimized solution but it allows us to solve BVP. To improve the convergence of the algorithm, it is necessary to incorporate a procedure for incrementing the inputs (i.e. displacement, acceleration, velocity, pore water pressures at the far-field side of the macro-element, or loading at pile-head) to limit the changes in the state of the macro-elements for each load increment. Therefore, instead of applying the input loads in one step (i.e. by computing time of 0.001 sec), the solution is divided into several time steps, and it proceeds with different increments adjusted by the state of the macro-elements owing to the assigned limitations.

6. Numerical Examples

To evaluate the performance of the macro-element model, two cases are investigated. One is the full-scale lateral load test on a 0.6 m cast-in-steel-shell (CISS) pile in sand liquefied by controlled blasting [22]. Another one is the centrifuge study of a pile supporting a single-degree-of-freedom superstructure induced by earthquake excitation [31]. Level-ground liquefaction (non-lateral-spreading) case is investigated in this fidelity analysis.

6.1. Full-scale field tests

A series of full-scale lateral load tests on the pile was carried out by [22] in sand liquefied by controlled blasting at Treasure Island in San Francisco Bay, California. The objective of the project was to assess the pile performance and soil response under pile-head cyclic loading during liquefaction. The cyclic loading was applied by a high-speed hydraulic actuator to the CISS pile. The CISS pile was also instrumented to allow for back-calculation of p–y curves. More details about site condition, loading sequence, instrumentation can be found in the original reference [22].

Sand layers deposited at Treasure Island are relatively loose and susceptible to liquefaction as observed following the 1989 Loma Prieta Earthquake [65]. Soil conditions were generally well defined across the island (see for example [66]). The results of the standard penetration test (SPT) and cone penetration test (CPT) conducted at the site are shown in Figure 11. $N_{1(60)}$ is the SPT N value corrected for field procedures and overburden pressure and q_c is the CPT tip resistance. The relative density (D_r) of the sand was estimated from the SPT and CPT results using relationships proposed by [62], and are also shown in Figure 11, indicating that the sand is loose to medium dense.

Friction angles were also estimated from $N_{1(60)}$ values using a correlation proposed by Peck et al. (1974) for comparison (Figure 11). It could also be obtained using a relationship with relative density (D_r) as proposed by the [38].

Flexural stiffness EI of the CISS pile is 291800 kN/m^2. Lateral loads were applied approximately 1.0 m above the excavated ground surface, and the total pile length is 14.8 m.

Liquefaction was induced by detonating the downhole explosives. The post-blast loading sequence consisted of ten separate load series to observe lateral pile and soil response over a range of excess pore water pressures. Liquefaction was observed during the first load series, where excess pore pressure ratios ranging between 70 and 100% near the pile (it is equivalent to macro-element level) and 30 to 90 % at a distance of 4.2 meters (far-field level) was observed. The post-blast loads were applied in half-cycles controlled by a varying maximum displacement target and an unloading displacement target. The cyclic loads were applied at a rate of approximately 10 mm/ s. The first series of loading cycles consisted of one 75 mm, one 150 mm, and one 225 mm displacement followed by ten more cycles at a displacement level of 225 mm.

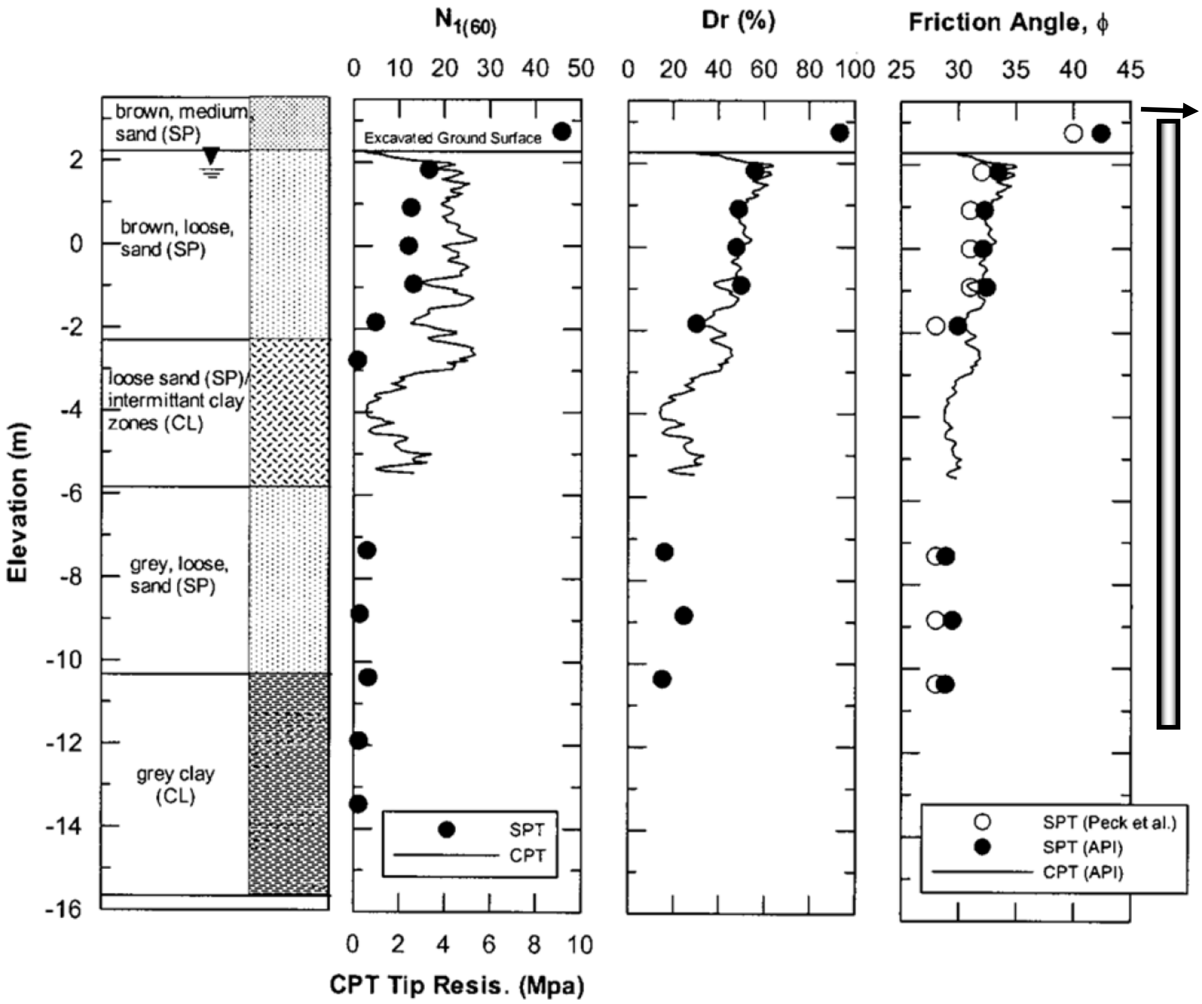

Figure 11. Soil profile, in-situ SPT and CPT tests results, relative density and friction angle obtained by in-situ test results. (after [22]*).*

The first series test targets the validation for this study. Figure 12 shows the Excess Pore Water Pressure (EPWP) variation around the pile and the distance of 4.2 m from the pile centre. As can be observed, variations of r_u is negligible around the pile and also at far-field for the first-test series. Hence the undrained loading condition is probably the best hypothesis for such a loading condition, and subsequent effects of S_{ff} is neglected and $dv = 0$.

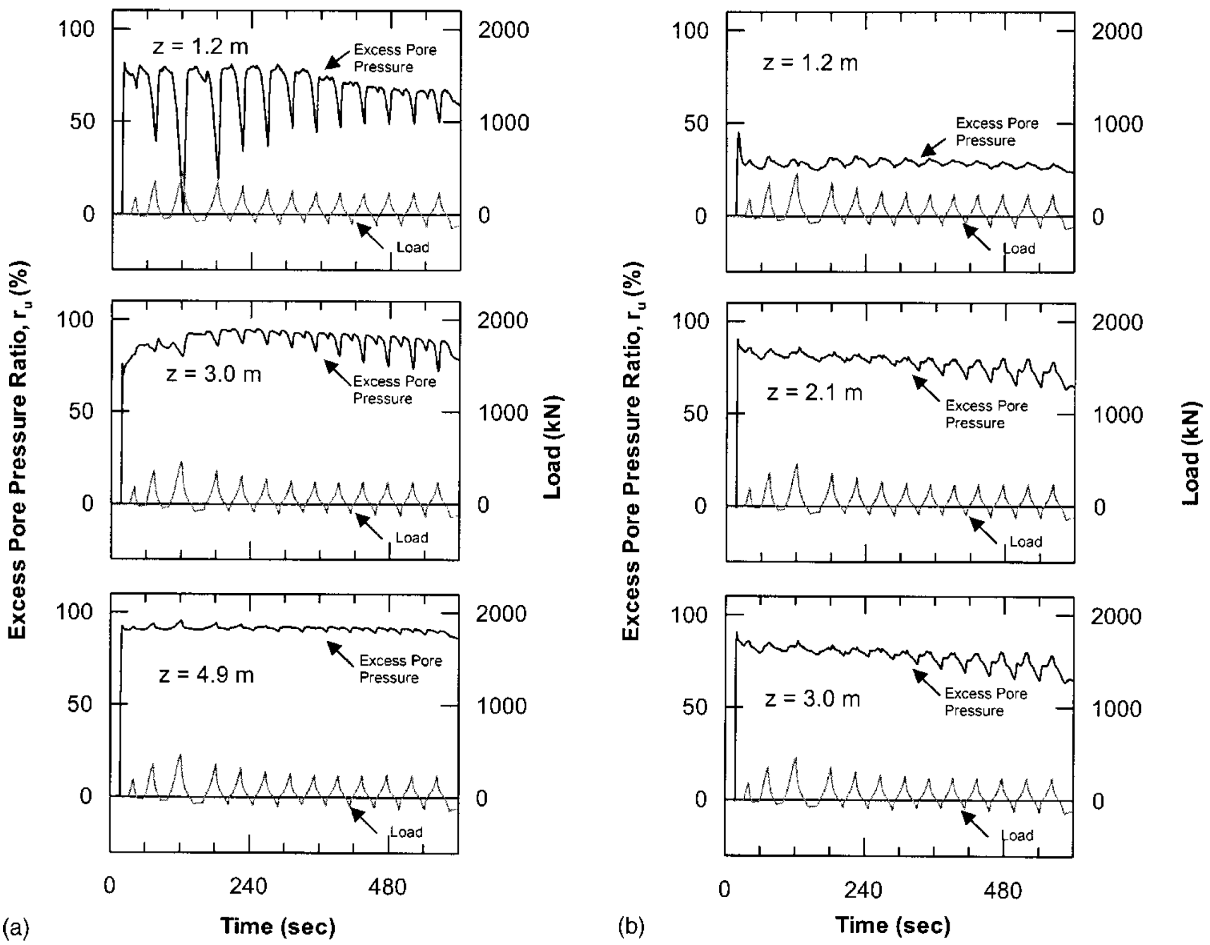

Figure 12. Excess-pore water pressure and the load versus time at (a) near the pile, (b) at a distance of 4.2 m from the pile centre. (after [22]*).*

The schematic of the macro-element model is shown in Figure 13. The soil parameters estimated from field data is calculated and they are provided in Table 2. In this study, the void ratio is obtained by relative density which is also a function of CPT tip-resistance (derived by [62]) as follows:

$$e = 2.05\left(D_{r(\%)}\right)^{-0.273} \quad 47$$

Initial value of the vertical soil resistance ($S = D_p \sigma'_v$) before blasting ($S_{0,i}$) is calculated by submerged unit weight. To consider the effects of the initial pore water pressure developed on the soil surrounding the pile into calculations, the initial value of the vertical soil resistance decreases. The amount of reduction is related to the excess pore water pressure ratio generated after blasting by the following equation:

$$S_0 = (1 - r_u)S_{0,i} \quad 48$$

where, r_u is the excess pore water pressure ratio in the vicinity of the pile, and it is shown in Figure 14. It is further assumed that the development of pore water pressure is negligible at the pile tip, and a linear relation exists between before and after blasting for the depth greater than 7 m. Owing to the observations made during the field test, r_u is about 0.7 to 1 at around 7 m of pile length. The average value (0.85) has been considered for calculating the initial state of the macro-element (Figure 14).

Table 2. The estimated soil parameters (initial parameters) for macro-elements.

Soil Type	Depth (m)	γ_{sat} (kN/m^3)	Relative Density D_r	Friction angle ϕ
Sand	0-0.2	19	60 %	37
Brown loose Sand	0.2-4.5	20	45 %	32
Clayey Sand (loose sand)	4.5-8.3	20	30 %	30
Grey loose Sand	8.3-13.8	20	30 %	29

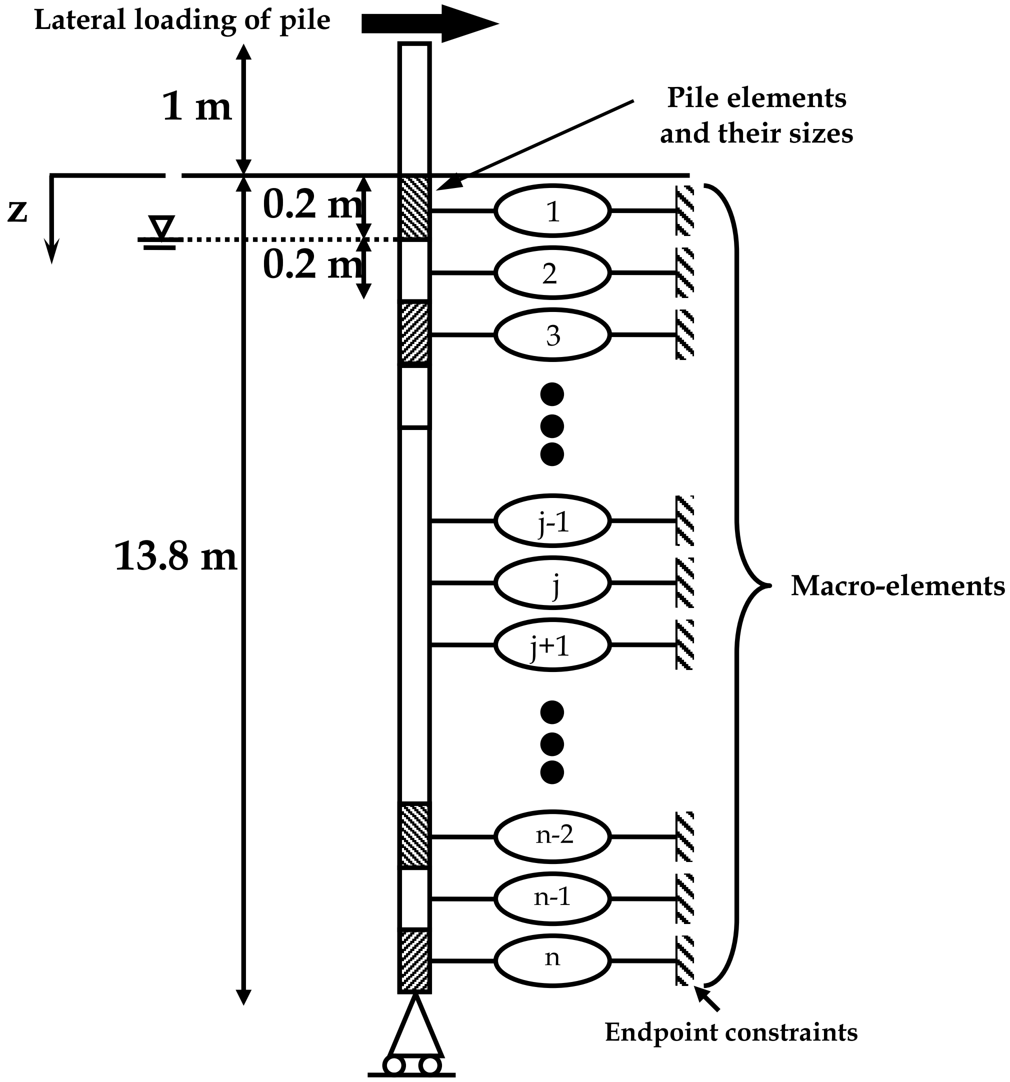

Figure 13. Statement of the problem in the macro-element.

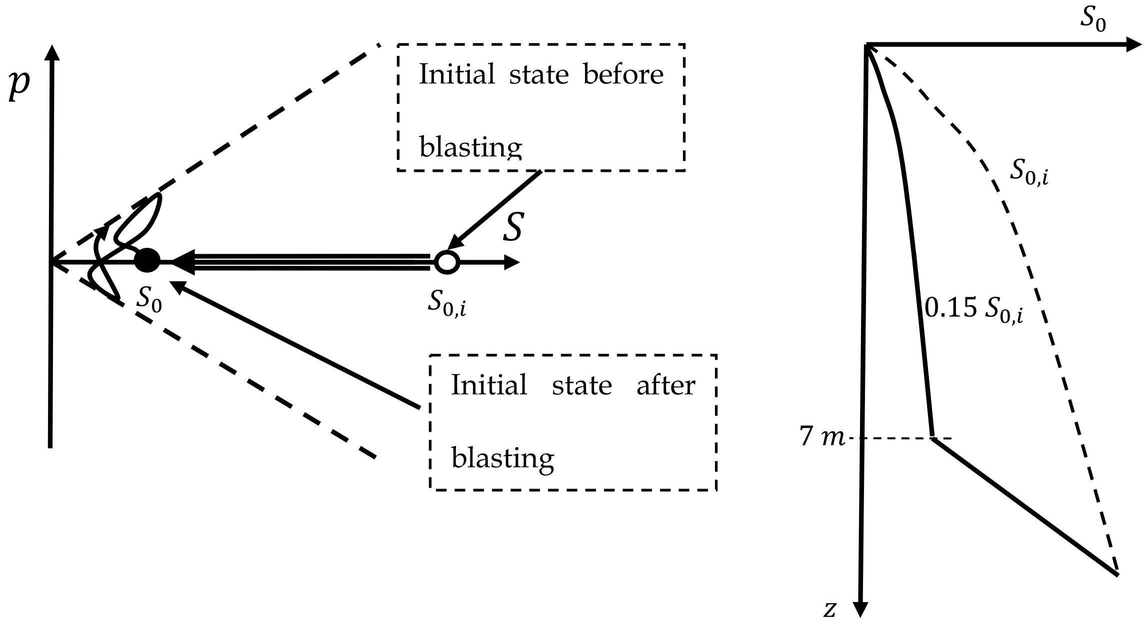

Figure 14. Initial state before and after blasting.

Using the initial soil parameters (Table 2) and making some realistic assumptions referring to the previous section, all model parameters are shown in Table 3.

Elastic Young modulus of soil is obtained by void ratio and mean effective stress (as reduced by a factor due to the current effective stress). G_0 is equal to the 1250 kPa constant for all soil types. It is worth mentioning that variations of G_0 have less effect on the results directly, because the initial state of the soil during the loading is mostly affected by nonlinearity. On the other hand, the elastic shearing and the volumetric stiffness of the macro-element are updated during loading by changing the vertical soil resistance (S). Hence the elastic stiffness reported in Table 3 is represented as a reference point. Updating the elastic stiffness is according to the following parabolic relation which is valid for sand as:

$$\begin{cases} K_s = K_{s0}\left(\dfrac{S}{S_r}\right)^{0.5} \\ \mathrm{N} = \mathrm{N}_0\left(\dfrac{S}{S_r}\right)^{0.5} \end{cases} \quad (49)$$

where, K_{s0} and N_0 are the reference elastic stiffnesses, and S_r is the reference vertical resistance of the macro-element. In this study, the reference point is assumed for the depth represented by the vertical soil resistance of $S_r = 2.6\ kPa/m$. $\alpha = 1.2$ is the constant assumed for the link between elastic Young modulus and shearing stiffness of the microelement.

The reference value of elastic volumetric stiffness of the soil-pile system is obtained by Eq. 35 where $\Upsilon = 0.112$. Since the soil has been influenced by blasting, the elastic volumetric stiffness is given by a large value.

The elastic volumetric stiffness and dilatancy are two significant parameters to simulate the accurate $p - y$ curve when the resistance path is moving on the limiting resistance surface, and it was explained by Eq. 25. The effect of dilatancy might be evaluated by two cases of variations of A_0 as: (1) parabolic variation, (2) homogeneous value (uniformly distributed). In this example, parabolic variation is chosen.

Table 3. Model parameters for validation of field test.

Model Parameters		value
Elastic	K_{s0}	$\alpha\ E_{s0}$
	N_0	140
Hardening Modulus	B_{min}	0.003
	B_{max}	0.01
	y_{c0}	0.2
Flow rule	A_0	$0.5\left(\frac{S}{S_r}\right)^{0.5}$
	λ_d	0.6
	χ	10
Residual resistance	S_{min}	0.05

Because the soil nonlinearity and the dilative response of the macro-element are more pronounced in this example, this clearly shows that the initial elastic shearing stiffness has very little effect on the pile-head response. The dilative stiffening of the soil, as an important character of the soil-pile model when slippage developed, is shown in both cases. Hence the material parameters exhibiting the flow rule behaviour is modelled very well.

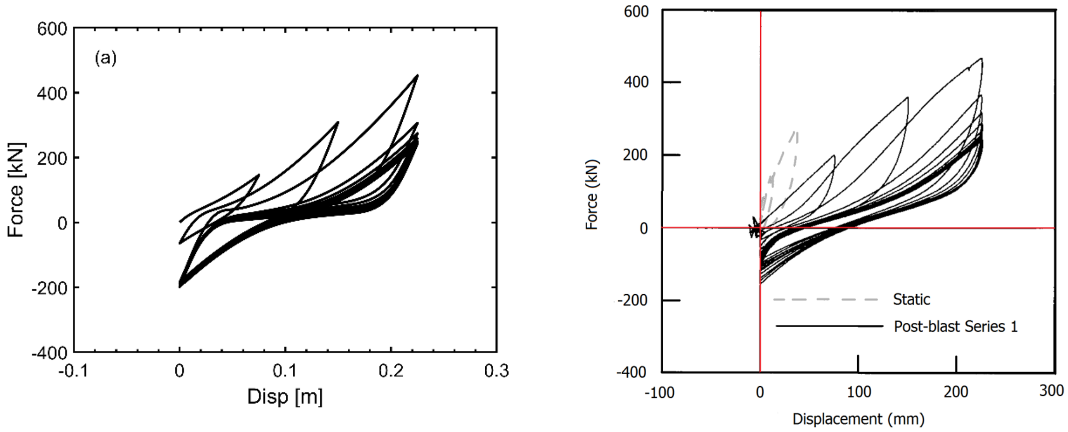

Figure 15. Lateral force-lateral displacement at top of the pile observed in (a) numerical simulations, (b) field tests [22].

Figure 15-a shows the load-displacement curve at the pile-head level. To compare the results of the current simulation and what observed in the field tests, Figure 15-b shows the lateral force-displacement in the field test. Two cases of the field test are shown in Figure 15-b as (1) static tests on pile head in pre-blasting condition, and (2) first series of post-blasting conditions. The dilative stiffening of the soil is the main character of pile-head response in post-blasting which is developed by the soil response in the pile vicinity. Reducing the lateral resistance by increasing the number of cycles applied on the pile-head is explained by the degradation of the soil resistance in the vicinity of the pile. The dilative stiffening of the soil surrounding the pile yields a unique inverted S shape on a load-displacement curve. The results of the current simulation are also exhibiting the dilative stiffening of the soil in a very good match with what was observed in the field test. The only difference between the current simulation (Figure 15-a) and the field test is about the hardening modulus parameters which would be altered. However, the current simulation is representing the pile-head response in a very good match for the whole range of loading sequences. To compare the force-displacement of the last cycle of the field test and the results of numerical simulation, Figure 16 is presented. The dilative stiffening of the macro-element is closely matched with the last

cycle of the field test. It shows a good simulation of the pile response when the slippage developed at the soil-pile interface in the post liquefaction phase of soil surrounding the pile.

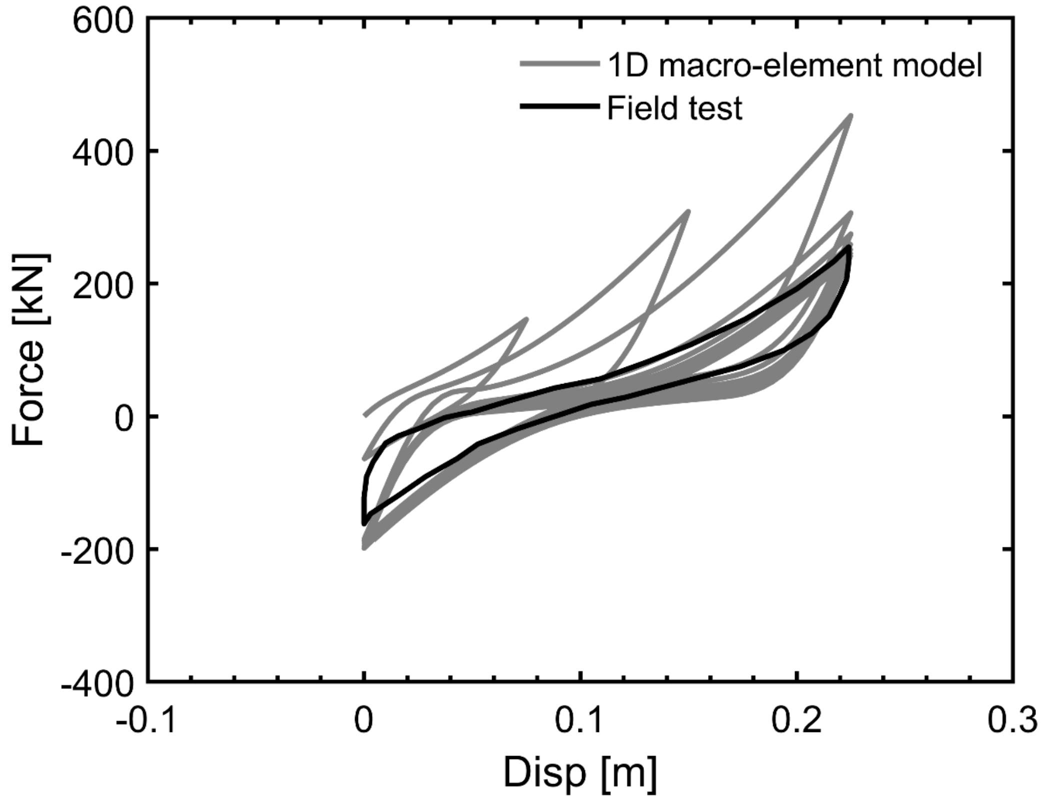

Figure 16. The comparison between simulated one and the last cycle of the field test.

To make a proper comparison between field test results and numerical simulation, p-y curves are shown in Figure 17. The field test results are exhibited by results of the last cycle only. As can be observed, the macro-element method shows promising results in comparison with the field test at shallow depths ($z \leq 3\ m$), but it predicts lower p-y curve responses at deeper layers. This would be refined by adopting higher A_0 and N_0 values at deeper layers. The agreement of the numerical simulations with the available field test indicates that the adopted macro-element technique for modelling the soil around the pile is appropriate for evaluating the pile response in the liquefiable ground.

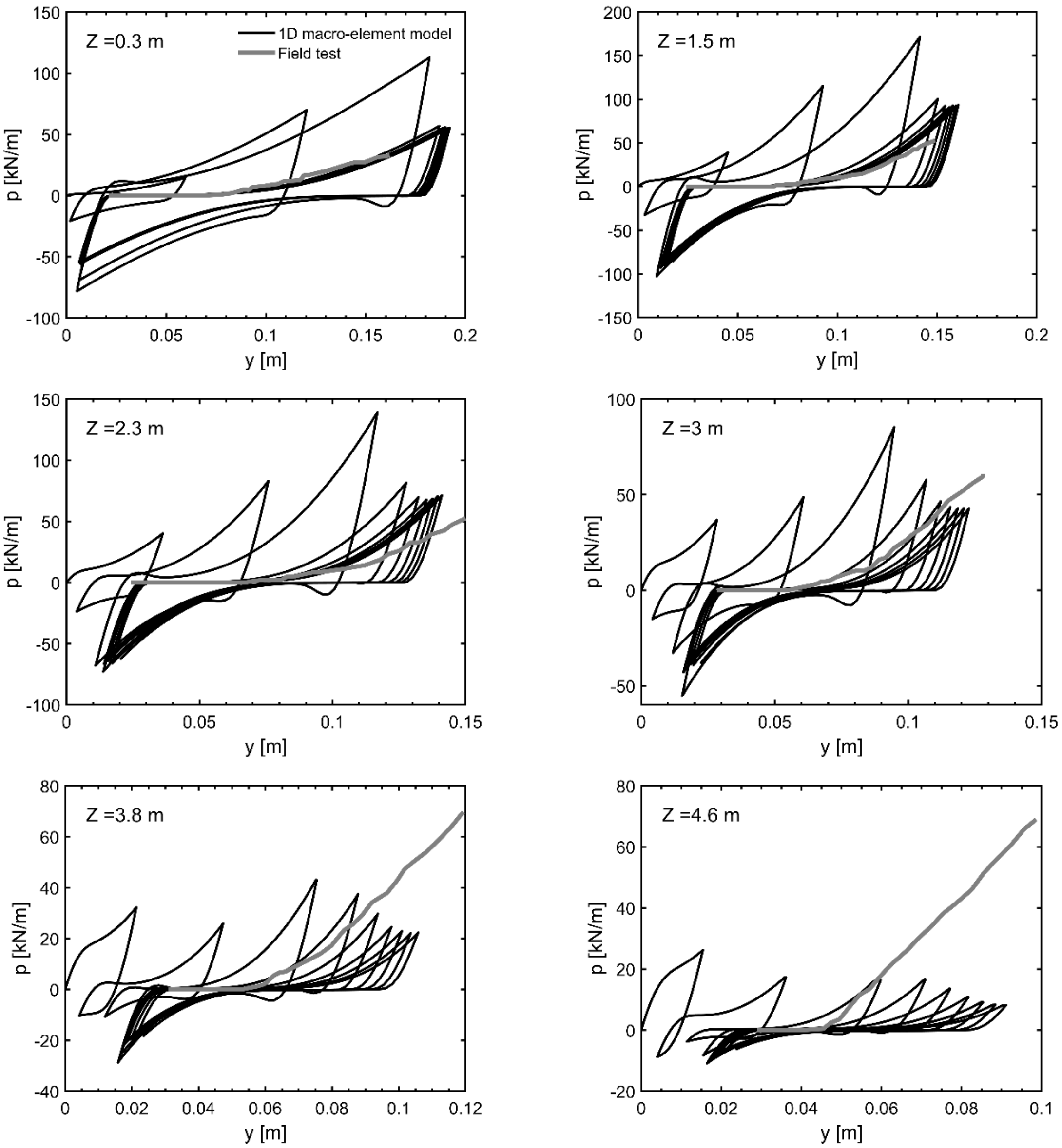

Figure 17. Comparison between p-y curves in the field test (last cycle), and the simulated one.

6.2. Dynamic Centrifuge Study

Test description

In this section, results of a centrifuge test on the single-pile foundation are investigated to demonstrate the capability of the macro-element for reliable analysis of piles under dynamic loading induced by earthquake and ground liquefaction. The dynamic centrifuge test of the pile-supported superstructure in liquefiable sand carried out by [31] is simulated.

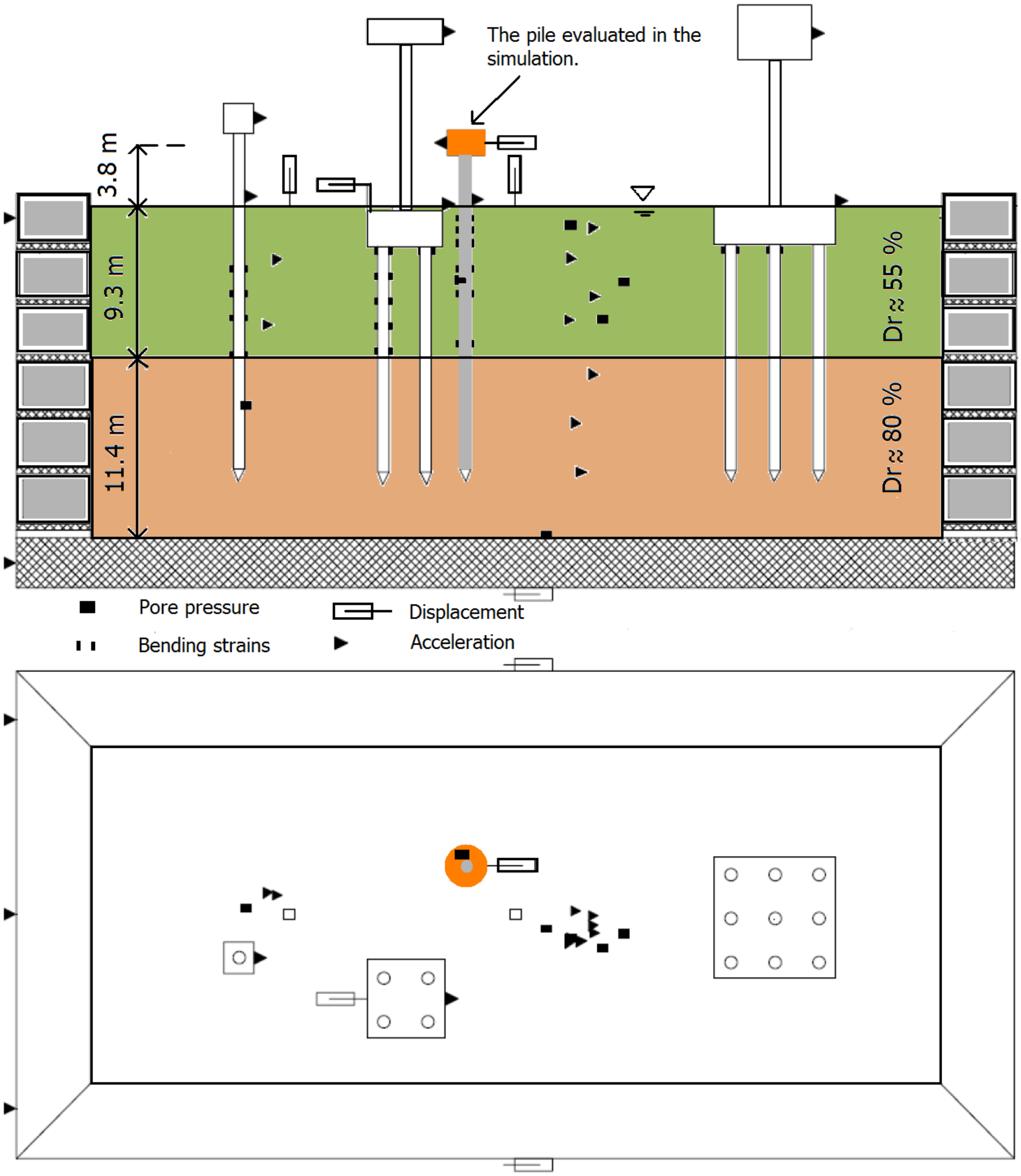

Figure 18. Model layout CSP_3 used in the simulation [31].

The particular configuration referred to as CSP_3 is chosen in this section. The soil profile consists of two layers of saturated, fine and uniformly graded Nevada sand (D_{50} = 0.15 mm, C_u = 1.5). Nevada sand is very fine, angular sand having a minimum void ratio of 0.511 and a maximum void ratio of 0.887. The saturated unit weight of the top layer and bottom layer are 19.81 and 20.4 kN/m^3. The lower dense layer (Dr = 80%) is 11.4 m thick, and the upper-medium dense layer (Dr = 55%) is 9.3 m thick at the prototype scale (Figure 18). The soil profile is saturated with a hydroxyl-propyl methyl-cellulose and water mixture whose viscosity is about 10 times greater than pure water. The centrifugal acceleration of 30 g was applied.

The single pile evaluated in the test is equivalent to a steel pipe pile with a diameter of 0.67 m, a wall thickness of 19 mm, and the embedded length of the pile is 16.8 m at the prototype scale. The pile is extended 3.8 m above the ground level and carries a superstructure load of 49.14 tons. To represent the typical bridge fundamental periods, column heights were selected to give fundamental periods for the structural systems ranging from 0.5 to 1.0 seconds [31]. The pile remained elastic during earthquake loading. The Aluminium pile model had an elastic Young's modulus of $E_p = 70\ GPa$.

The model was subjected to Event-J which the acceleration record of the Kobe 1995 is scaled to 0.22 g and used as an input motion. The base input acceleration is shown in Figure 19.

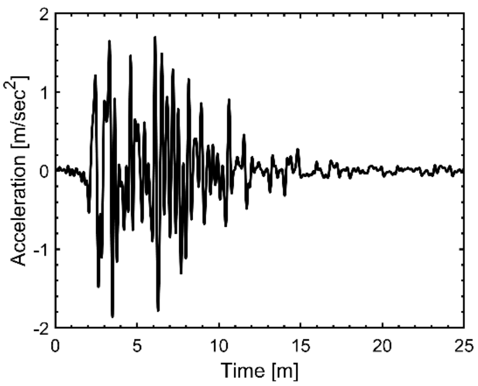

Figure 19. Input earthquake ground motion (Acceleration record of Kobe (1995) scale to PGA of 0.22 g).

1D macro-element modelling

Figure 20 shows the statement of this problem. Displacement, velocity, acceleration, and EPWPR time series at far-field are input parameters to the macro-elements. This is carried out by an additional FEM employing OPENSEES and Pressure dependent Multi-yield surface model (PDMY02) developed by Elgamal and his colleagues [67]. Material parameters of the Nevada sand were derived by [68] for a 3D column of soil and Tcl code is available online in the author's GitHub repository: https://github.com/mshadlou/macroelement). This part is used for site response investigation and it is very quick to run. Considering a column of soil at far-field, the above inputs to the macro-element are calculated by linear interpolations between measured data (accelerations and pore-water pressures) to provide better resolution.

Displacement and velocity time series of the centrifuge study are obtained by double and single integration over acceleration time series accompanying the butterwort filtering to maintain the residual/permanent displacements. As shown in Figure 18, 7 accelerometers and 5 pore-water pressure transducers were being used to record the accelerations and pore-water pressure at the far-field in the centrifuge study.

To optimize the time of calculation in this dynamic analysis, the sub-stepping algorithm is used. The recording time of the simulation is 0.01 seconds, and the original computation time step is 0.001. The penalty time step is limited to 1×10^{-8} sec.

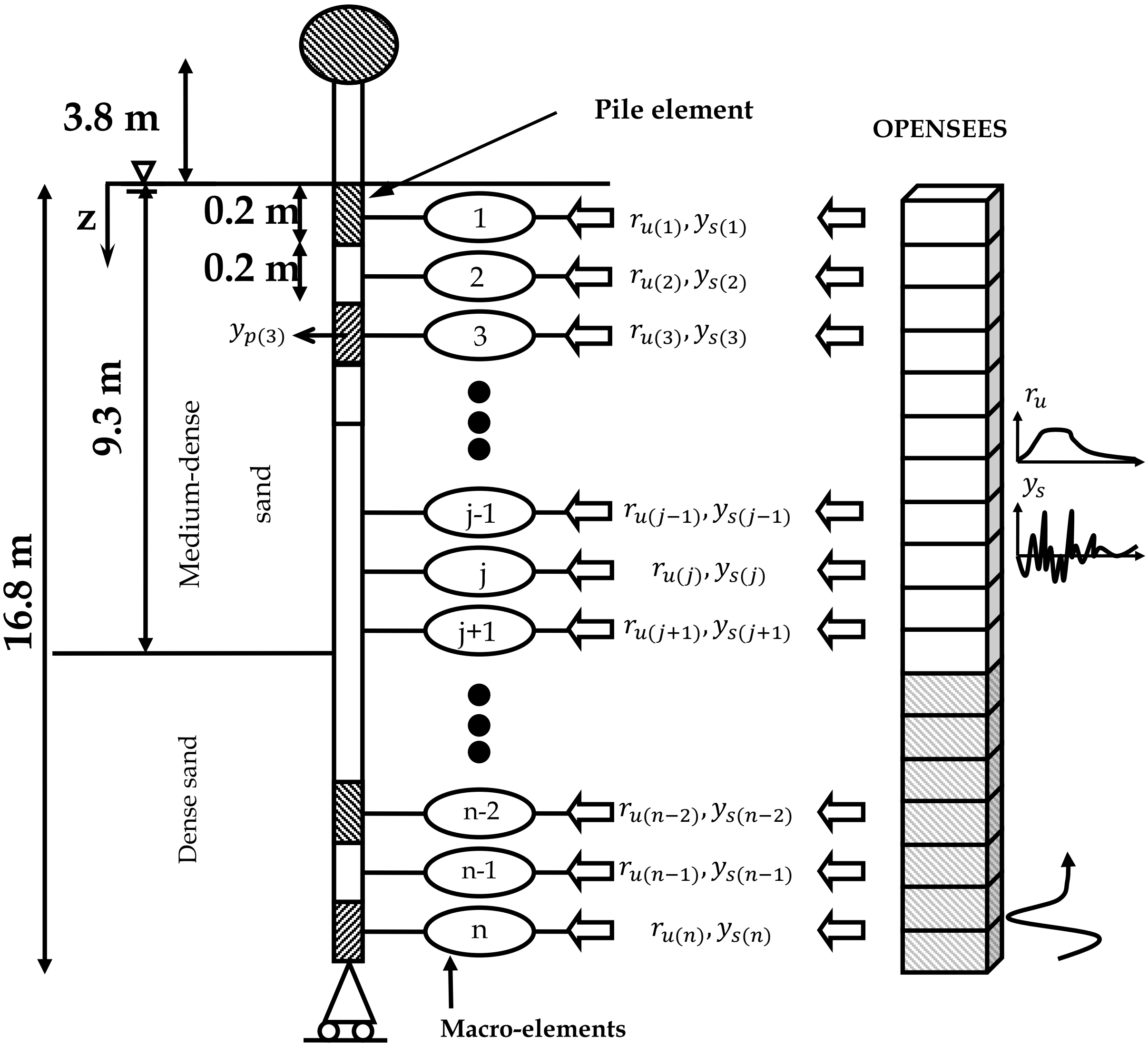

Figure 20. Statement of the problem in the simulation.

Soil Properties and Material Parameters

Maximum elastic shear modulus of Nevada sand is calculated by Eq. 9 where, $F_{(\vartheta)}$ is as following for angular grains [43]:

$$F_{(\vartheta)} = \frac{(3.97 - \vartheta)^2}{\vartheta} \qquad 50$$

Soil material parameter (G_0) is assumed 400 (obtained by recasting the shear modulus represented by [67]), and the power exponent (n) is 0.7. Peak friction angle of Nevada sand for two relative densities used in tests are; (1) $\phi = 34^0$ in the case of $Dr = 55\ \%$, and (2) $\phi = 38^0$ in the case of $Dr = 80\ \%$. Critical state friction angle of Nevada sand is 30^0. In this case, dilatancy surface and subsequently λ_d may be simply calculated by Eq. 40. Elastic stiffness of macro-elements is updated by the same equation presented in the previous example (Eq. 49), in which the reference vertical soil resistance is 3.5 kPa/m, and power exponent (n) is 0.7. Elastic shearing stiffness factor (α) is calculated by the method presented by [49]. The superstructure is vibrated by a unitary force (with 1N amplitude) and the displacement of the same level is calculated by the elastodynamic solution. The predominant period of the system is 0.73 sec as shown in Figure 21. To calibrate α, different values have been tried and the predominant period of the soil-pile-superstructure system in the macro-element approach was calculated. Results are shown in Figure 22. To have the same predominant period (T_o) between continuum solution and the macro-element approach, $\alpha = 2$ is selected.

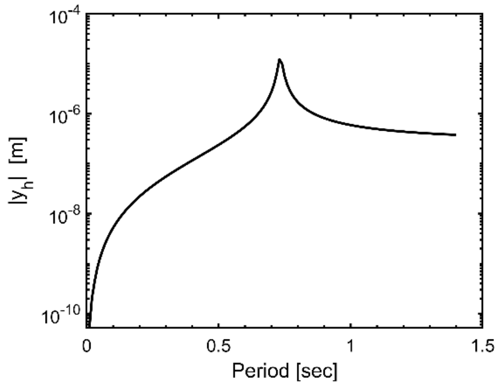

Figure 21. Calculated predominant period of the soil-pile-superstructure system using elastodynamic solution [49].

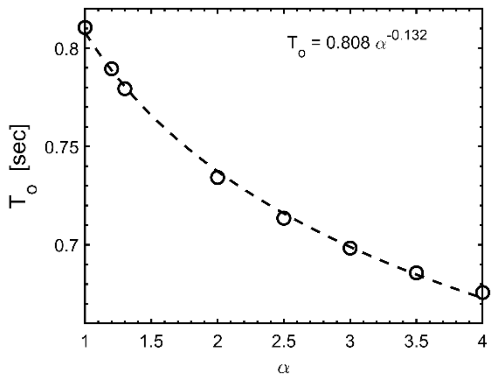

Figure 22. Sensitivity of predominant period of the system in the Macro-element approach to elastic stiffness factor, a.

Since the soil-pile system is influenced by the dynamic loading-unloading-reloading process, the Poisson's ratio is 0.2 (the same concept is usually used in the constitutive modelling of soil, i.e. [69], [70]).

Material parameters for this study are listed in Table 4. The reference elastic volumetric stiffness (N_0) is set to be $\mathrm{N}_0 = 10$. To provide a gradual reduction in the dilative response of the macro-elements from the top to the bottom of the ground, the following exponential equation has been proposed to characterize variations of A_0 with depth:

$$A_0 = \left(A_{0,1} - A_{0,2}\right) \exp(-0.1S) + A_{0,2} \tag{51}$$

where, $A_{0,1}$ and $A_{0,2}$ are the representative values at ground level and deep layers, respectively. As explained before, A_0 is obtained by the slope of the stress-dilatancy line during a drained loading condition in the laboratory experiment. This value presents the rate of developing pore water pressure in a layer hence it is well-expected that the higher value must be assigned on top and a lower value is set for bottom layers. [67] assigned contraction parameter (c_1) and dilation parameter (d_1), which both more or less have the same concept of A_0, as 0.18 and 0.5 for 40 % relative density and 80 kPa mean effective stress for Nevada sand. These values shed some light on the possible range of A_0 for further applications.

Since the upper-saturated-soil layers meet the onset of liquefaction quicker than the bottom layers, χ is set to be higher for upper layers and lower for bottom layers. An exponential equation is used to fit the variations of χ with depth (or vertical resistance) as following equation (similar to Eq. 51):

$$\chi = 490 \exp(-0.1S) + 10 \tag{52}$$

The hardening modulus is obtained by Eq. 19 and substituting B_{min}, B_{max} and y_{c0} with 0.0009, 0.002 and 0.3 m, respectively. This stiffness-proportional nonlinear damping model is used and calculated with the aid of Eq. 32. Figure 23 shows the variations of C_r with depth. As it can be seen, a sharp change of radiation damping is observer on interface between two layers.

Table 4. Model parameters for simulating the centrifuge study.

Model Parameters		value
Elastic	K_{s0}	$\alpha\ E_{s0}$
	N_0	10
Hardening Modulus	B_{min}	0.0009
	B_{max}	0.002
	y_{c0}	0.3
Flow rule	A_0	Eq. 51 $\begin{cases} A_{01} = 0.3 \\ A_{02} = 0.2 \end{cases}$
	λ_d	$\begin{cases} \lambda_{d1} = 0.636 \\ \lambda_{d2} = 0.5141 \end{cases}$
	χ	Eq. 52
Residual resistance	S_{min}	0.5 (kPa/m)
Radiation Damping	C_r	Eq. 32 0.5 C_r

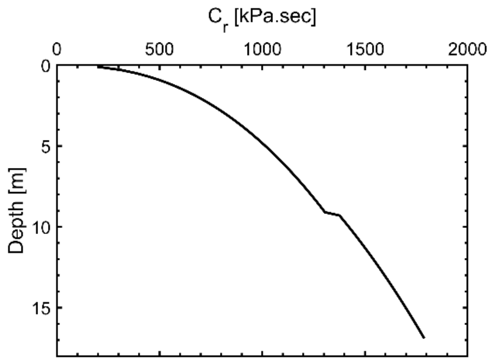

Figure 23. Variations of the radiation damping coefficient (C_r) with the depth.

Superstructure and pile responses

The acceleration time series at the superstructure level and the pile head and the displacement time series at the superstructure are shown in Figure 24. It can be observed that the current simulation has provided a good match with what is observed in the dynamic centrifuge study.

Figure 25 shows the bending moment time series in some particular depths. The agreement between the macro-element modelling and the centrifuge study in shallow to deep layers is quite good in this simulation. The transient and post-liquefaction bending moments influenced by the steady-state response are simulated very well.

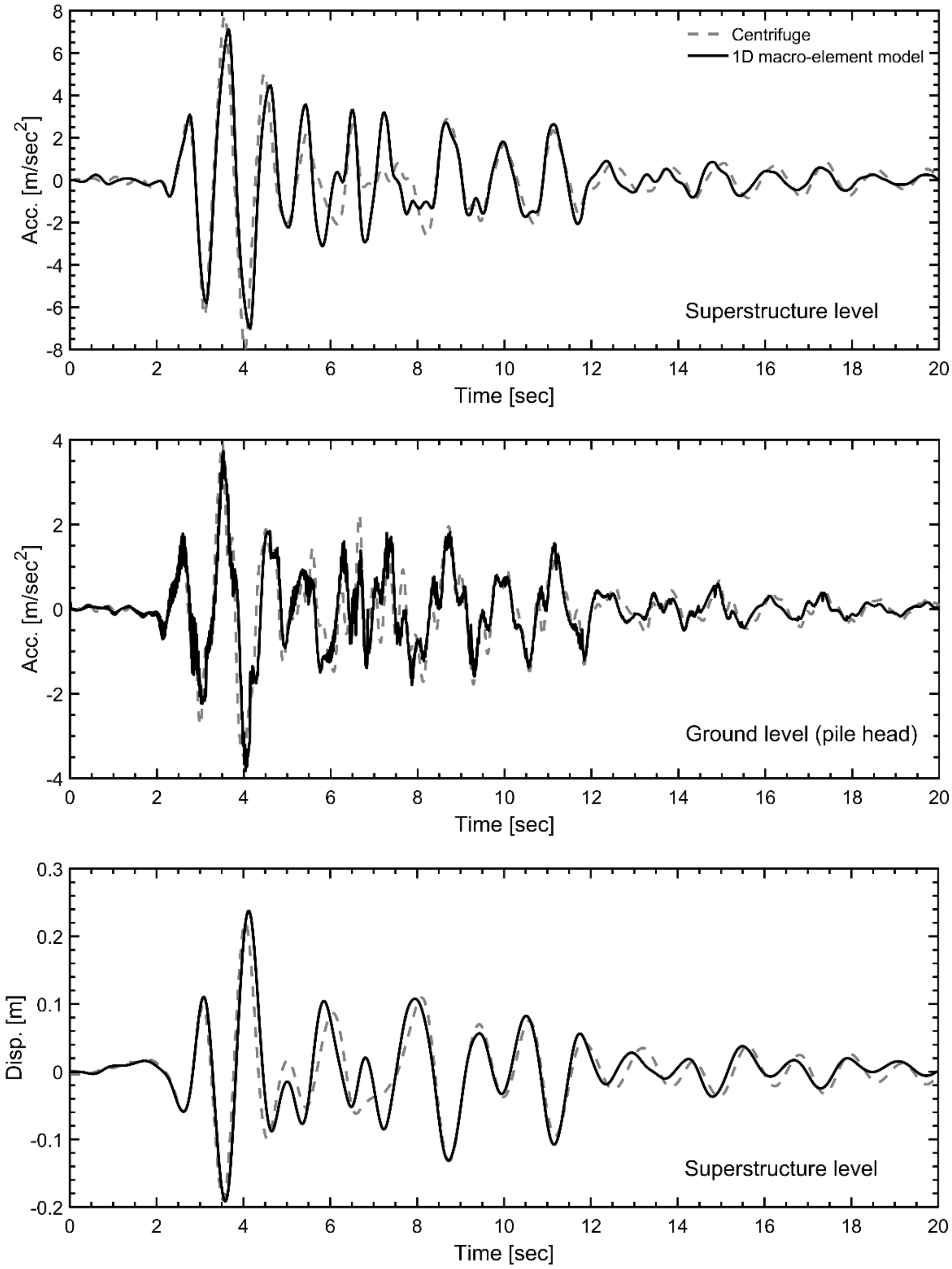

Figure 24. Accelerations and displacement at the superstructure level and the pile-head.

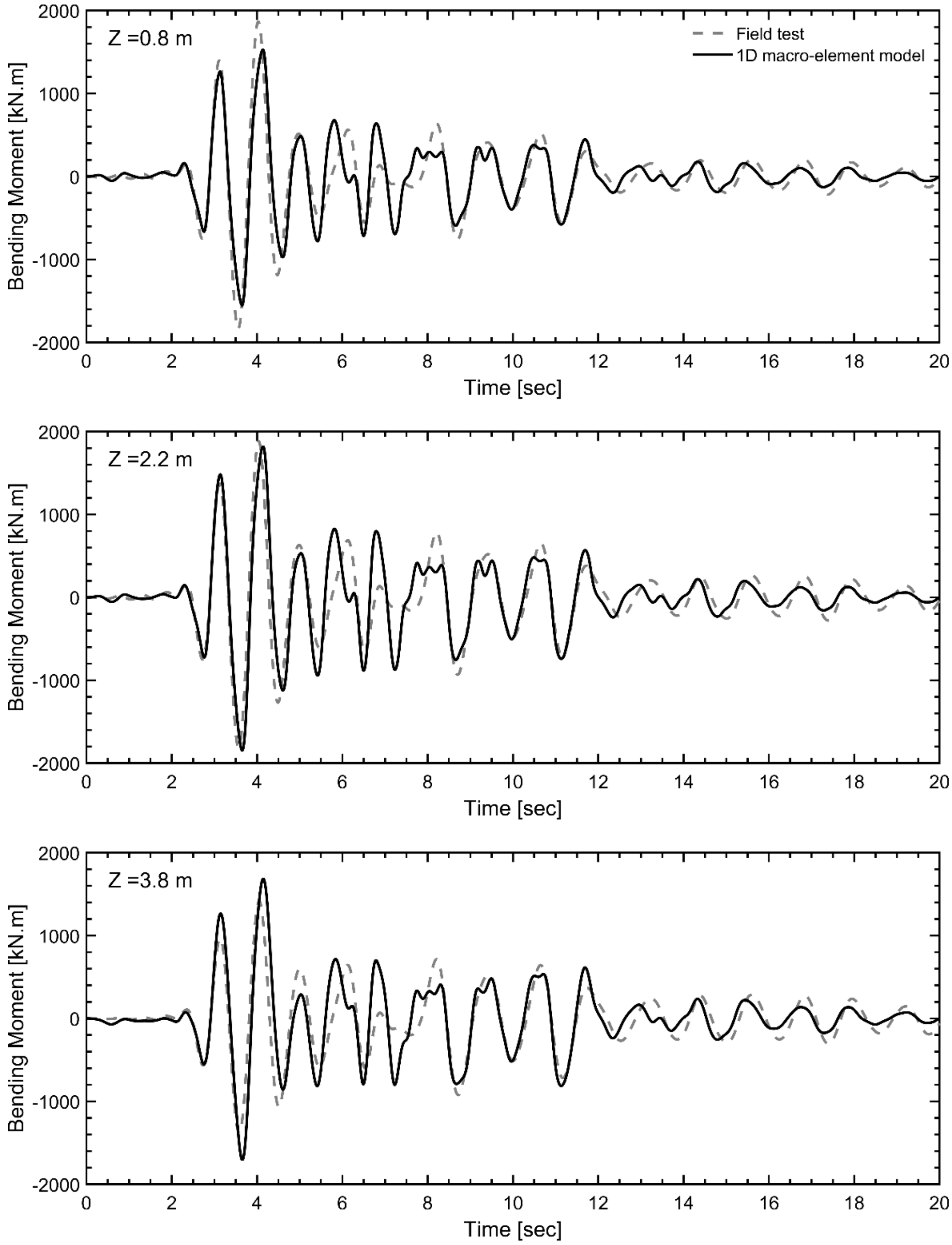
Z =0.8 m
Field test
1D macro-element model
Bending Moment [kN.m]
Time [sec]
Z =2.2 m
Bending Moment [kN.m]
Time [sec]
Z =3.8 m
Bending Moment [kN.m]
Time [sec]

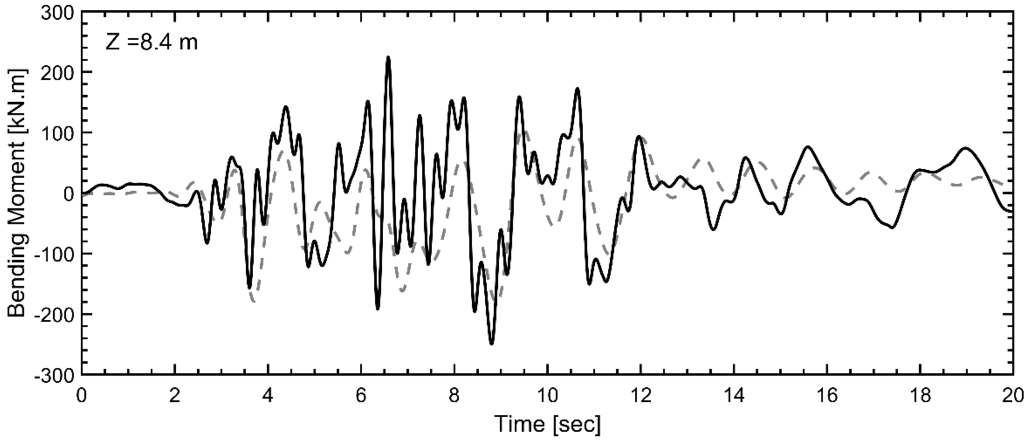

Figure 25. The observed and simulated bending moment time series.

Figure 26 compares the maximum bending moment profiles in the macro-element and centrifuge study. The error between the maximum bending moment observed on the pile in the centrifuge study and one obtained in the macro-element is circa 3 per cent. It is also shown that the macro-element approach predicts the location of bending moment slightly deeper than one observed in the centrifuge study.

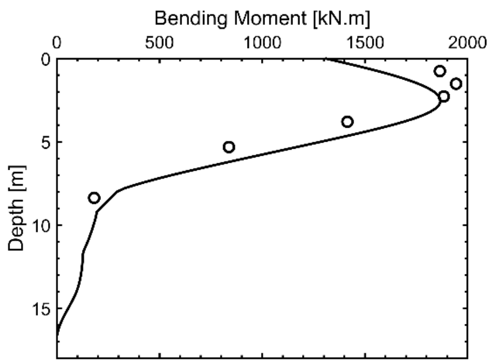

Figure 26. Comparison between the maximum-simulated-bending-moment profile and the one observed in the centrifuge study.

Obtaining $p - y$ curves

The next step is to compare $p - y$ curves back-calculated from the centrifuge study [31] and those obtained by the macro-element approach. Back calculated $p - y$ curves are obtained by measured bending moments on pile, hence, if there is nearly 100 percent agreement between measured and simulated bending moments, then the observed $p-y$ curves should be somehow similar to simulated ones. As shown in simulated cases (Figure 25 and Figure 26), observed bending moments and simulated ones have good agreements. Double integration and double derivation of bending moments in respect of depth are needed to back-calculate $p-y$ curves. Hence the key point for this process is the number of measured bending strains along the pile. Sensitivity to noises, boundary conditions, method of interpolation (integration and differentiation), and signal processing techniques are counted as other parameters influencing the back-calculated $p-y$ curves in centrifuge study. This is not observed in numerical modelling and $p-y$ are directly obtained by the macro-element.

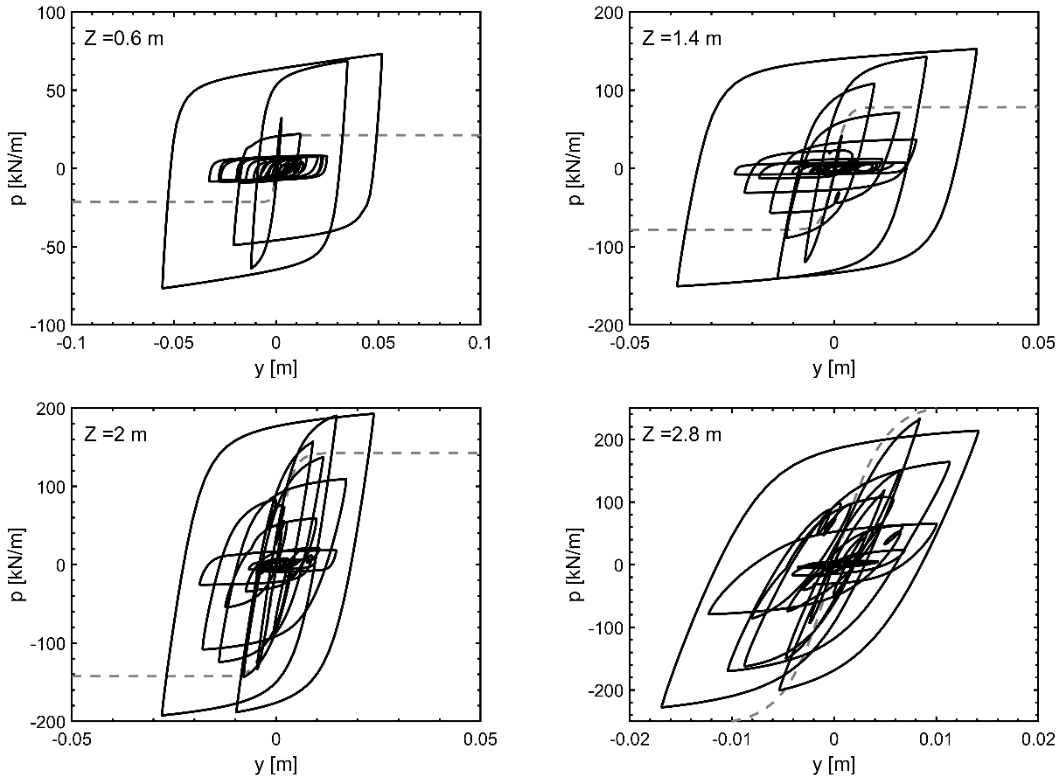

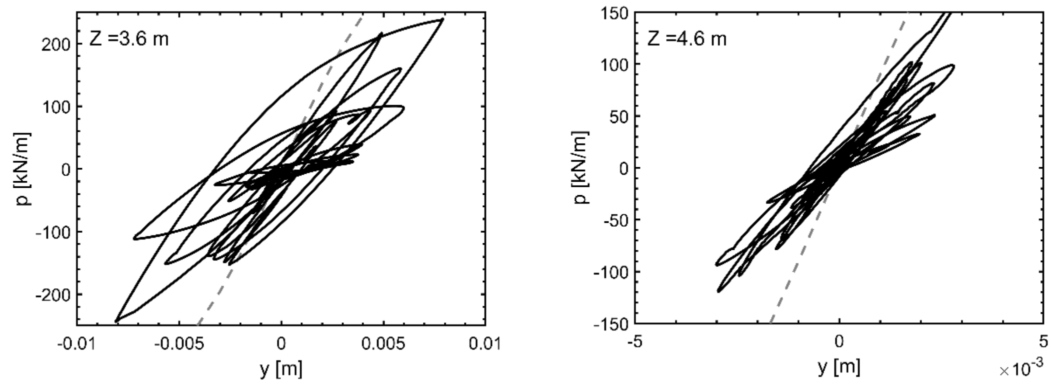

Figure 27. p-y curves in some particular depths in the macro-elements (black-solid line) and its comparison with the API p-y curves (dashed-grey line).

Figure 27 and Figure 28 show the $p-y$ curves obtained by the macro-element model and back-calculated ones [31], respectively. Despite a good agreement between bending moment along with the pile, pile head displacement and superstructure accelerations and displacement, the $p-y$ curves are quite different. It concludes the less sensitivity of pile response to the $p-y$ curves, however more dilative macro-elements might yield to the better answer. To compare these $p-y$ curves with those suggested by [38], the grey line is exhibited in Figure 27. It is shown that upper layers are influenced by the dilative response of the macro-element and subsequently limiting resistances are achieved and the expected soil resistance will be lower than values recommended by API. This condition is not seen in bottom layers as soil nonlinearity would not be considered on the depth of more than 5 m. Following the above conclusions, adopting the higher dilative coefficient, A_0 and the lower radiation damping might yield a better result.

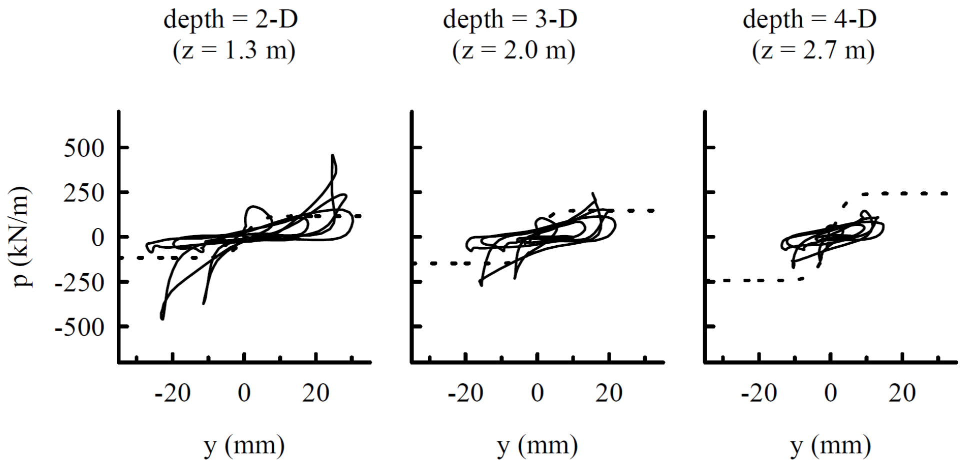

Figure 28. Back-calculated p-y curves [31].

7. An application for 1D macro-modelling

Dynamic characteristics of a system covering period and damping are notable parameters facilitating the design process. They are usually estimated by code of practices (e.g. ASCE 7-10 [71], Eurocode 8 [72]) for a soil-structure interaction system. Investigating the instantaneous period of a system is usually taken place by signal processing of a recorded signal such as acceleration on the superstructure ([73]) while the damping is estimated using a transfer function linking two time-series in the frequency domain. This raises another difficulty when the nonlinearity is employed in the system and our aim is at estimating the damping of the superstructure only.

The second-order differential equation of a dynamic system in the macro-element approach (Eq. 41) contains global mass, stiffness and damping matrices. Because of the nonlinearity of macro-elements and the non-associated flow rule of the plasticity method, it is a non-classically damped system. To obtain natural periods, damping ratios, and modal shapes, the method presented in Appendix 1 [74] is used by solving the quadratic eigenvalue problem. The numerical simulation presented in section 6.2 is evaluated in this section.

Figure 29-a and Figure 29-b show the instantaneous period and damping ratio of the first mode of the system. The period is elongated (up to 1.3 sec) by 1.6 times the initial value (0.73 sec) at the end of loading. The period is elongated over the first four seconds, decreases at around 4.5 to 5.5 seconds and then gradually increases. As shown, the instantaneous period gradually increases despite fluctuation around its median value. The damping ratio also increases despite having been specially introduced after the first 4 seconds of loading simultaneously with decreasing the period. The fluctuation of the damping ratio is also observed in Figure 29-b. As shown, the period gets the minimum in a single time step and the damping ratio is given the maximum value at the same time. This is explained due to dilative stiffening of the macro-elements which increase both the stiffness of the soil-pile system and the damping ratio. Hence the natural period of the system increases. Unlike dilative stiffening, softening of soil due to reduction of the vertical resistance of soil (*S*) yields to increasing the period and reducing the damping. This may also be explained by initial elastic radiation damping in the unloading process.

To evaluate the performance of the method, one would be comparing the instantaneous first mode period of the system calculated by quadratic eigenvalue solution and one obtained by wavelet energy spectrum ([73], [75], [13], [36]) of the acceleration time series recorded at superstructure as shown in Figure 30. The predominant periods (represented by the highest energy point at each instance) of recorded accelerations are very similar to the periods in Figure 29-a. The only differences are observed between 8 to 10 seconds when the recorded motion exhibits a more predominant period (around 1.4 to 1.5 sec.).

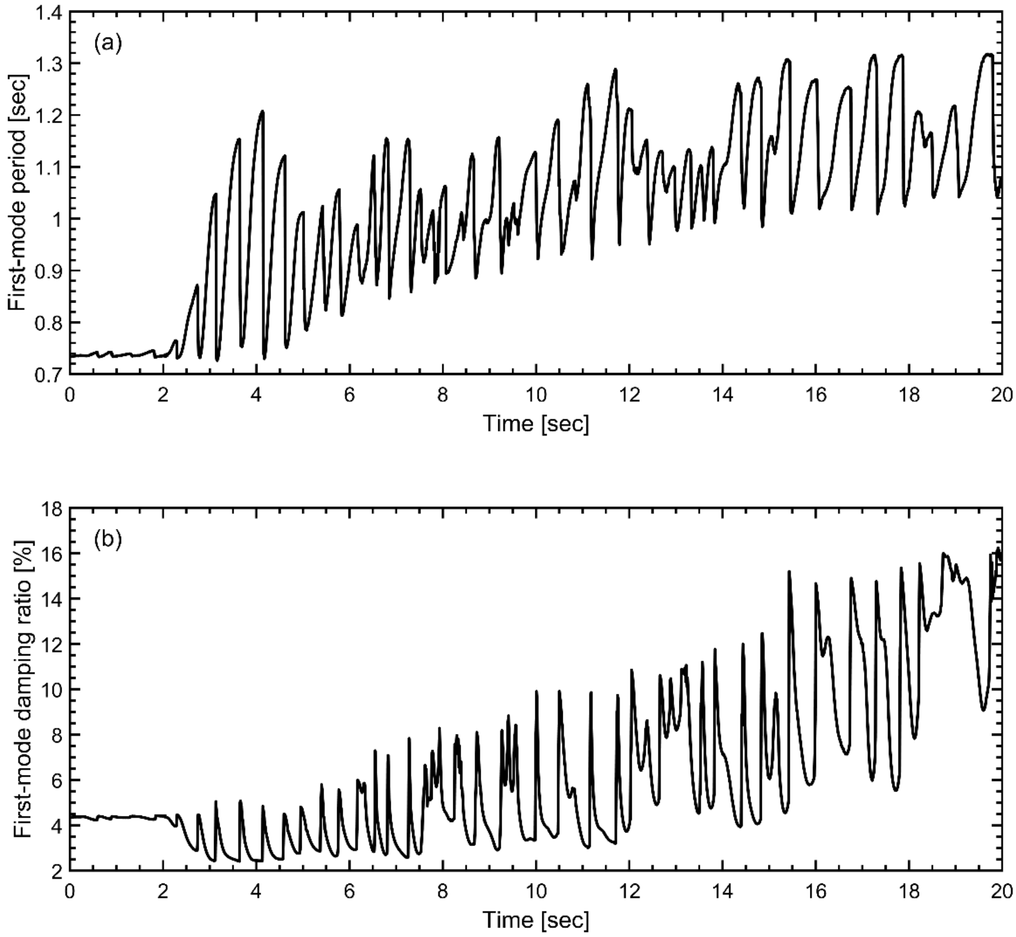

Figure 29. (a) Instantaneous-first mode period and (b) instantaneous-first mode damping ratio of the system obtained by quadratic eigenvalue solution.

Unfortunately, there is no method to assess the accuracy of the damping ratio unless we use the presented method and rely on engineering judgements, concerning the current knowledge of authors. Using $G-\gamma$ curve and $\xi-\gamma$ curve (ξ stands for damping ratio) for most of the sands obtained by dynamic shear tests and resonant column tests, it is derived that the damping ratio of the soil would be up to 10 to 20 % at large shear strains hence damping ratio of the system evaluated in this research would be in the right range. While the current research shows that damping is fluctuating, as a result of dilations in macro-element, using conventional $\xi-\gamma$ curve would not solely be a reliable design option.

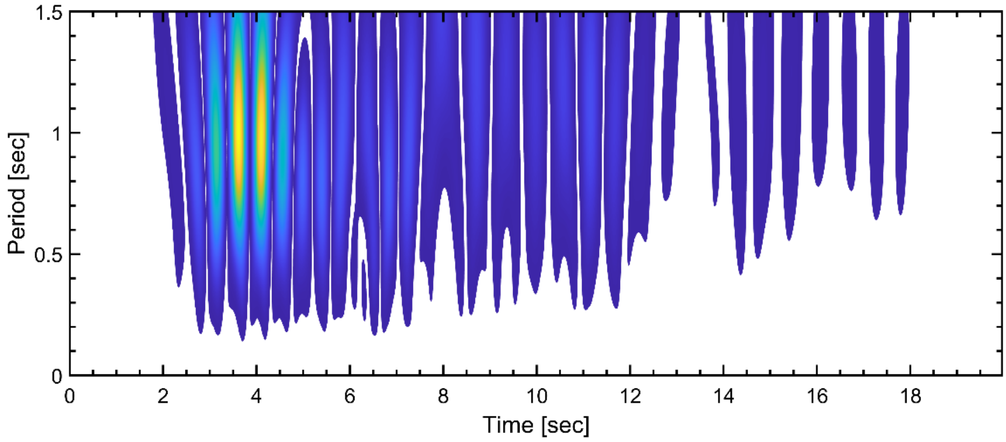

Figure 30. Wavelet energy spectrum of acceleration recorded on the superstructure.

8. Conclusion

New and existing superstructures (such as bridges and buildings) supported on pile foundations and located in sites susceptible to liquefaction and lateral spreading are required to be assessed or designed to withstand the actions of extreme loads. Hence it is necessary to simulate the soil-pile system using a reliable method supported by realistic soil constitutive relations surrounding the pile. There is a trade-off between simplified 1D models and complex FE models. This study is suggesting a 1D macro-element model which is only tuned by soil properties and can capture the complex mechanism of the soil-pile system in the liquefiable ground.

The agreement of the numerical simulations with the available field test and centrifuge modelling indicates that the adopted macro-element technique for modelling the soil around the pile is appropriate and promising for evaluating the pile response in the liquefiable ground.

The presented macro-element is replaced with the soil surrounding the pile and simulate the actual soil behaviour. A hypo-elastic bounding surface model was developed in the framework of the macro-element to underpin and facilitate the future concerns of resilience-based design of infrastructures built on piles in the liquefiable and laterally spreading ground.

Soil resistance (p, which is known in $p-y$ curve) is initially decomposed into its possible ingredients: (i) p_y (limiting soil resistant) is explained for frictional material such as sand, (ii) an average-effective resistance (S) was introduced, (iii) $p-S$ relation in addition to $p-y$ relation was explained, (iv) specifications for another variable to address the volumetric constraints of the soil surrounding the pile were put in place. The later is associated with radial change of an RVE of soil around the pile. As a result, two surface tractions (p and S)[N/m] and two displacement components (one is associated with pile disp. and another one is associated with radial change of RVE) [m] were presented. According to a hypothesised-dissipation mechanism, the dilation mechanism of macro-element was explained. Then the solution in FEM of pile was instituted in contrast with conventional FEMs in which the soil elements are also modelled and computational time/cost increases. As the number of macro-elements are limited, local integration is used on limited number of elements in contrast with full soil-pile FEMs.

One application for the presented 1D modelling approach was given by calculating the instantaneous period and damping ratio of the system (soil-pile interaction system) simulating a centrifuge study. It showed that the resolution of period and damping changes are higher than signal processing techniques having limited applications. Due to dilative stiffening of the macro-elements, both the stiffness of the soil-pile system and the damping ratio increases hence period decreases at the same instance. Representing the high damp system for soil-pile interaction mechanism in the liquefiable soil won’t be the right choice for design purposes.

This research presented a fast and robust approach suitable for thousands of analyses aiming at spatial viability, performance-based design, risk assessment, fragility analysis as well as resilient-based design; these are the suggested future works.

Data Availability Statement

Some or all data, models, or code generated or used during the study are available from the corresponding author by request. Tcl code for site response analysis using Opensees is available online in the author's GitHub repository: https://github.com/mshadlou/macroelement.

Acknowledgement

The authors acknowledge the support received by the UK Engineering and Physical Sciences Research Council (EPSRC) for grant numbers EP/H015345/1 and EP/H015345/2.

Appendix 1: Quadratic eigenvalue solution

For non-classically damping system as being considered in the 1D macro-element approach under dynamic loading condition, second order differential equation can be converted into its quadratic eigenvalue forms by the following equation:

$$Q_{(\lambda)} = \lambda^2 I + \lambda\, M^{-1} C I + \lambda\, M^{-1} K I \qquad \text{A-1}$$

where, $\lambda = \omega_n\left(\xi + i\sqrt{|1-\xi^2|}\right)$ is eigenvalue containing natural frequency (ω_n) and damping ratio (ξ). I is an identity matrix. This problem can be solved by linearization in the following form:

$$T_{(\lambda)} = A - \lambda B \qquad \text{A-2}$$

where,

$$A = \begin{bmatrix} M^{-1}KI & 0 \\ 0 & I \end{bmatrix}, B = \begin{bmatrix} -\lambda\, M^{-1}CI & -I \\ I & 0 \end{bmatrix} \qquad \text{A-2}$$

Then an eigensolver can be used (for example MATLAB function eig) to solve this generalized eigenproblem. A most elaborated version of the linearization technique is recently proposed by [76].

References

[1] Muir Wood D. Soil mechanics: a one-dimensional introduction. Cambridge, UK: Cambridge University Press; 2009.

[2] Zienkiewicz OC, Chan a. HC, Pastor M, Schrefler B a., Shiomi T. Computational Geomechanics with Special Reference to Earthquake Engineering. 2001.

[3] Yang Z, Jeremić B. Numerical analysis of pile behaviour under lateral loads in layered elastic-plastic soils. International Journal for Numerical and Analytical Methods in Geomechanics 2002;26:1385–406. https://doi.org/10.1002/nag.250.

[4] Dobry R, Thevanayagam S, Abdoun T, Elgamal A, El Shamy U, Zeghal M. Study of pile response to lateral spreading using physical testing and computational modeling. 4th International Conference on Earthquake Geotechnical Engineering, 2007.

[5] Rahmani A, Taiebat M, Liam Finn WD. Nonlinear dynamic analysis of Meloland Road Overpass using three-dimensional continuum modeling approach. Soil Dynamics and

Earthquake Engineering 2014;57:121–32. https://doi.org/10.1016/j.soildyn.2013.11.004.

[6] Wang R, Fu P, Zhang JM. Finite element model for piles in liquefiable ground. Computers and Geotechnics 2016;72:1–14. https://doi.org/10.1016/j.compgeo.2015.10.009.

[7] Li G, Motamed R. Finite element modeling of soil-pile response subjected to liquefaction-induced lateral spreading in a large-scale shake table experiment. Soil Dynamics and Earthquake Engineering 2017;92:573–84. https://doi.org/10.1016/j.soildyn.2016.11.001.

[8] Su L, Lu J, Elgamal A, Arulmoli AK. Seismic performance of a pile-supported wharf: Three-dimensional finite element simulation. Soil Dynamics and Earthquake Engineering 2017;95:167–79. https://doi.org/10.1016/j.soildyn.2017.01.009.

[9] Badry P, Satyam N. An efficient approach for assessing the seismic soil structure interaction effect for the asymmetrical pile group. Innovative Infrastructure Solutions 2016;1. https://doi.org/10.1007/s41062-016-0003-1.

[10] Rajeswari JS, Sarkar R. Estimation of Transient Forces in Single Pile Embedded in Liquefiable Soil. International Journal of Geomechanics 2020;20:06020023. https://doi.org/10.1061/(asce)gm.1943-5622.0001788.

[11] Tran NX, Bong T, Yoo BS, Kim SR. Evaluation of the soil–pile interface properties in the lateral direction for seismic analysis in sand. Soil Dynamics and Earthquake Engineering 2021;140:106473. https://doi.org/10.1016/j.soildyn.2020.106473.

[12] Dobry R. Simplified methods in Soil Dynamics. Soil Dynamics and Earthquake Engineering 2014;61:246–68. https://doi.org/10.1016/j.soildyn.2014.02.008.

[13] Bhattacharya S, Tokimatsu K, Goda K, Sarkar R, Shadlou M, Rouholamin M. Collapse of showa bridge during 1964 niigata earthquake: a quantitative reappraisal on the failure mechanisms. Soil Dynamics and Earthquake Engineering 2014;65:55–71.

[14] Knappett JA, Madabhushi SP. Influence of axial load on lateral pile response in liquefiable soils. II: numerical modelling. Geotechnique 2009;59:583–592.

[15] Liyanapathirana DS, Poulos HG. Analysis of pile behaviour in liquefying sloping ground. Computers and Geotechnics 2010;37:115–24. https://doi.org/10.1016/j.compgeo.2009.08.001.

[16] Brandenberg SJ, Zhao M, Boulanger RW, Wilson DW. p-y Plasticity Model for Nonlinear Dynamic Analysis of Piles in Liquefiable Soil. Journal of Geotechnical and Geoenvironmental Engineering 2013;139:1262–74. https://doi.org/10.1061/(asce)gt.1943-5606.0000847.

[17] Varun, Assimaki D, Shafieezadeh A. Soil-pile-structure interaction simulations in liquefiable soils via dynamic macroelements: Formulation and validation. Soil Dynamics and Earthquake Engineering 2013;42:92–107. https://doi.org/10.1016/j.soildyn.2012.03.008.

[18] Choi JI, Kim MM, Brandenberg SJ. Cyclic p-y Plasticity Model Applied to Pile Foundations in Sand. Journal of Geotechnical and Geoenvironmental Engineering 2015;141. https://doi.org/10.1061/(asce)gt.1943-5606.0001261.

[19] Knappett JA, Madabhushi SP. Influence of axial load on lateral pile response in liquefiable soils.part I: physical modelling. Geotechnique 2009;59:571–581.

[20] Lombardi D, Dash SR, Bhattacharya S, Ibraim E, Muirwood D, Taylor CA. Construction of simplified design p–y curves for liquefied soils. Geotechnique 2017;67:216–27. https://doi.org/10.1680/jgeot.15.P.116.

[21] Ashford SA, Rollins KM. The treasure island liquefaction tests: final report. San Diego: 2002.

[22] Weaver TJ, Ashford SA, Rollins KM. Response of 0.6m Cast-in-Steel-Shell Pile in Liquefied Soil under Lateral Loading. Journal of Geotechnical and Geoenvironmental Engineering 2005;131:94–102. https://doi.org/10.1061/(asce)1090-0241(2005)131:1(94).

[23] Iai S. Analysis of soil deformation around a cylinderical rigid body. US-Japan seminar on seismic disaster mitigation in urban area by geotechnical engineering, 2002.

[24] Yasuda S, Yoshida N, Kiku H, Adachi K. A simplified method to evaluate liquefaction-induced deformation. In: Pinto PS, editor. Earthquake Geotechnical Engineering, 1999, p. 555–66.

[25] Sato H, Hamada M, Doi M. An experimental study of effects of laterally flowing ground on in-ground structures,. In: O'Rourke, T.D., Hamada M, editors. 5th Japan-US workshop on Earthquake Resistant Design of Lifeline Facility and Countermeasures agains Soil Liquefaction, 1994, p. Technical Report NCEER-94-0026.

[26] Towhata I, Vargas-Monge W, Orense RP, Yao M. Shaking table tests on subgrade reaction of pipe embedded in sandy liquefued subsoil. Soil Dynamics and Earthquake Engineering 1999;18:347–61.

[27] Takahashi A. Soil – pile interaction in liquefaction-induced lateral spreading of soils. 2002.

[28] Dash S. Lateral pile-soil interaction in liquefiable soil. University of Oxford, Oxford, England, 2010.

[29] Tokimatsu K, Suzuki H. Pore water pressure response around the pile and and its effects on p-y behaviour during soil liquefaction. Soils and Foundations 2004;44:101–10.

[30] Gonzalez L, Abdoun T, R. Dobry. Effect of soil permeability on centrifuge modeling of pile response to lateral spreading. ASCE Journal of Geotechnical and Geoenvironemental Engineering 2009;135:62–73.

[31] Wilson DW. Soil-pile-superstructure interaction in liquefying sand and soft clay. Doctoral Dissertation, University of California, Davis 1998.

[32] Boulanger RW, Kutter BL, Brandenberg SJ, Singh P, Chang D. Pile foundations in liquefied and laterally spreading ground during earthquake: centrifuge experiments and analyses. 2003.

[33] Motamed R, Towhata I, Honda T, Tabata K, Abe A. Pile group response to liquefaction-induced lateral spreading: E-defence large shake table test. Soil Dynamics and Earthquake Engineering 2013;51:35–46.

[34] Forcellini D. Analytical fragility curves of pile foundations with soil-structure interaction (SSI). Geosciences (Switzerland) 2021;11:1–19. https://doi.org/10.3390/geosciences11020066.

[35] Shadlou M, Bhattacharya S. Dynamic stiffness of monopiles supporting offshore wind turbine generators. Soil Dynamics and Earthquake Engineering 2016;88:15–32.

[36] Shadlou M. Contribution to static and dynamic response of piles in liquefiable ground. University of Bristol, 2016.

[37] Matlock H. Correlations for design of laterally loaded piles in soft clay. Proceedings of the Annual Offshore Technology Conference, 1970, p. 577–94.

[38] API. Recommended Practice for Planning , Designing and Constructing Fixed Offshore Platforms — Working Stress Design. Api Recommended Practice 2007.

[39] Reese LC, Cox WR, Koop FD. Analysis of laterally loaded piles in sand. Proceedings of the Annual Offshore Technology Conference, 1974, p. 473–85. https://doi.org/10.4043/2080-ms.

[40] Boulanger RW, Curras CJ, Kutter BL, Wilson DW, Abghari A. Seismic Soil-Pile-Structure Interaction Experiments and Analyses. Journal of Geotechnical and Geoenvironmental Engineering 1999;125:750–9. https://doi.org/10.1061/(asce)1090-0241(1999)125:9(750).

[41] Houlsby GT. How the dilatancy of soils affects their behaviour -done. International Proceedings of the 10th European Conference on Soil Mechanics and Foundation Engineering 1991.

[42] Lehane BM, Gaudin C, Schneider JA. Scale effects on tension capacity for rough piles buried in dense sand. Geotechnique 2005;55:709–19. https://doi.org/10.1680/geot.2005.55.10.709.

[43] Hardin B, Richart F. Elastic Wave Velocities in Granular Soils. Journal of the Soil Mechanics and Foundations Division 1963;89:33–65.

[44] Towhata I. Geotechnical Earthquake Engineering. 1st ed. Bwelin: Springer-Verlag Berlin Heidelberg; 2008.

[45] Taylor DW. Fundamentals of soil mechanics. 1st ed. New York: John Wiley; 1948.

[46] Gajo A, Muir Wood D. Severn-Trent sand: a kinematic-hardening constitutive model: the q± p formulation. Geotechnique 1999;49:595–614.

[47] Oka F, Yashima A, Tateishi A, Taguchi Y, Yamashita S. A cyclic elasto-plastic constitutive model for sand considering a plastic-strain dependence of the shear modulus. Geotechnique 1999;49:661–80. https://doi.org/10.1680/geot.1999.49.5.661.

[48] JRA. Specifications for Highway Bridges, Part V, Seismic Design. Kapan Road Association; 2002.

[49] Shadlou M, Bhattacharya S. Dynamic stiffness of pile in a layered elastic continuum. Geotechnique 2014;64:303–19.

[50] Perzyna P. The constitutive equations for rate sensitive plastic materials. Quarterly of Applied Mathematics 1963. https://doi.org/10.1090/qam/144536.

[51] Gerolymos N, Gazetas G. Phenomenological model applied to inelastic response of soil-pile interaction systems. Soils and Foundations 2005;45:119–32. https://doi.org/10.3208/sandf.45.4_119.

[52] Allotey N, El Naggar MH. Generalized dynamic Winkler model for nonlinear soil-structure interaction analysis. Canadian Geotechnical Journal 2008;45:560–73. https://doi.org/10.1139/T07-106.

[53] Broms B. Lateral Resistance of Piles in Cohesionless Soils. Journal of the Soil Mechanics and Foundations Division 1964;90:123–56.

[54] Poulos HG, Davis EH. Pile Foundation Analysis and Design. New York: John Wiley; 1980.

[55] Fleming K, Weltman A, Randolph M, Elson K. Piling Engineering. 2008. https://doi.org/10.1201/b22272.

[56] Barton O. Laterally Loaded Model Piles in Sand: Centrifuge Tests and Finite Element Analyses. Cambridge, UK: University of Cambridge; 1986. https://doi.org/10.17863/CAM.31170.

[57] Hatanaka M, Uchida A. Empirical Correlation Between Penetration Resistance and Internal Friction Angle of Sandy Soils. Soils and Foundations 1996;36:1–10. https://doi.org/10.3208/sandf.36.4_1.

[58] Robertson PK, Campanella RG. Interpretation of cone penetration tests. Part II: clay. Canadian Geotechnical Journal 1983;20:718–33. https://doi.org/10.1139/t83-079.

[59] Roscoe KH, Schofield AN, Thurairajah A. Yielding of Clays in States Wetter than Critical. Geotechnique 1963;13:211–40. https://doi.org/10.1680/geot.1963.13.3.211.

[60] Ishihara K, Tatsuoka F, Yasuda S. UNDRAINED DEFORMATION AND LIQUEFACTION OF SAND UNDER CYCLIC STRESSES. Soils and Foundations 1975;15:29–44. https://doi.org/10.3208/sandf1972.15.29.

[61] Bolton MD. The strength and dilatancy of sands. Geotechnique 1986;36:65–78. https://doi.org/10.1680/geot.1986.36.1.65.

[62] Kulhawy FH, Mayne PW. Manual on Estimating Soil Properties for Foundation Design. Ostigov 1990.

[63] Chopra A. Dynamics of Structures; Theory and Applications to Earthquake Engineering. 2nd ed. New Jersey: Printice Hall; 1995.

[64] Newmark NM. A method of computation for structural dynamics. Journal of Engineering Mechnaics Division, ASCE 1959;85:69–74.

[65] Power MS, Egan JA, Shewbridge S, DeBecke J. Analysis of liquefaction-induced damage on treasure island. In: Holzer T, editor. The Lorna Prieta, California, Earthquake of October 17, 1989-Liquefaction, Washington: 1997, p. 87–119.

[66] Faris JR, de Alba P. National Geotechnical Experimentation Site at Treasure Island, California. National Geotechnical Experimentation Sites, 2000. https://doi.org/10.1061/9780784404843.ch03.

[67] Elgamal A, Yang Z, Parra E, Ragheb A. Modeling of cyclic mobility in saturated cohesionless soils. International Journal of Plasticity 2003;19:883–905. https://doi.org/10.1016/S0749-6419(02)00010-4.

[68] Khosravifar A. Analysis and design for inelastic structural response of extended pile shaft foundations in laterally spreading ground during earthquakes. University of California, Davis, 2012.

[69] Dafalias YF, Manzari MT. Simple Plasticity Sand Model Accounting for Fabric Change Effects. Journal of Engineering Mechanics 2004;130:622–34.

[70] Loukidis D, Salgado R. Modeling sand response using two-surface plasticity. Computers and Geotechnics 2009;36:166–86.

[71] ASCE. ASCE/SEI 7-10: Minimum Design Loads for Buildings and Other Structures. Virginia, USA: 2010.

[72] CEN. Eurocode 8: Design of structures for earthquake resistance. 2004.

[73] Zhou Z, H. Adeli. Wavelet energy spectrum for time-frequency localization of earthquake energy. International Journal of Imaging Systems and Technology 2003;13:133–140.

[74] Francoise T, Meerbergen K. The quadratic eigenvalue problem. SIAM REVIEW 2001;43:235–286.

[75] Emadi A, Shakib H, Shadlou M. Investigation of beneficial and detrimental effects of soil-foundation-structure interaction on the seismic response of shear buildings. KSCE Journal of Civil Engineering 2014;18:253–263.

[76] Hammarling S, Munro CJ, Tisseur F. An Algorithm for Complete Solution of Quadratic Eigenvalue Problems. ACM Transactions on Mathematical Software 2013;39:1–19.